

# Comparing 1-year GUMICS–4 simulations of the Terrestrial Magnetosphere with Cluster Measurements

G. Facskó<sup>1,2,3</sup>, D. G. Sibeck<sup>2</sup>, I. Honkonen<sup>4</sup>, J. Bór<sup>5</sup>, G. Farinas Perez<sup>2,3\*</sup>,  
A. Tímár<sup>1</sup>, Y. Y. Shprits<sup>6,7</sup>, L. Degener<sup>4†</sup>, P. Peitso<sup>8‡</sup>, E. I. Tanskanen<sup>8</sup>,  
C. R. Anekallu<sup>9</sup>, J. Kalmár<sup>5</sup>, S. Szalai<sup>5,10</sup>, Á. Kis<sup>5</sup>, V. Wesztergom<sup>5</sup>,  
N. A. Aseev<sup>6,7</sup>

<sup>1</sup>Wigner Research Centre for Physics, Budapest, Hungary

<sup>2</sup>NASA Goddard Space Flight Center, Greenbelt, Maryland, USA

<sup>3</sup>the Catholic University of America, Washington DC, USA

<sup>4</sup>Finnish Meteorological Institute, Helsinki, Finland

<sup>5</sup>Research Centre for Astronomy and Earth Sciences, Sopron, Hungary

<sup>6</sup>Helmholtz Centre Potsdam, GFZ German Research Centre for Geosciences, Potsdam, Germany

<sup>7</sup>Institute for Physics and Astronomy, University of Potsdam, Potsdam, Germany

<sup>8</sup>Aalto University, School of Electrical Engineering, Espoo, Finland

<sup>9</sup>UCL Department of Space & Climate Physics, Mullard Space Science Laboratory, Dorking, UK

<sup>10</sup>University of Miskolc, Department of Geophysics, Miskolc, Hungary

## Key Points:

- The GUMICS–4 code provides realistic ion plasma moments and magnetic field in the solar wind and the outer magnetosheath.
- The code [...] predicts [...] realistic bow shock locations [...].
- An inner magnetosphere model should be added to the code to increase the accuracy of the simulation.

\*Now at University of Miami, Electrical and Computer Engineering Department, Miami, Florida, USA

†Now private individual, Hannover, Germany

‡Now at Aurora Propulsion Technologies, Espoo, Finland

Corresponding author: Gábor Facskó, gabor.i.facsko@gmail.com

23      **Abstract**

24      We compare the predictions of the GUMICS-4 global magnetohydrodynamic  
 25      model for the interaction of the solar wind with the Earth's magnetosphere  
 26      with Cluster-3 measurements over the course of one year, from January 29,  
 27      2002 to February 2, 2003. In particular, we compare the predictions with the  
 28      north/south component of the magnetic field ( $B_z$ ), the component of the ve-  
 29      locity along the Sun-Earth line ( $V_x$ ), and the plasma density as determined  
 30      from a top hat plasma spectrometer and the spacecraft's potential. We select  
 31      intervals in the solar wind, the magnetosheath and the magnetosphere where these in-  
 32      struments above provided good quality data and the **model correctly predicts the**  
 33      **region in which the spacecraft is located**. We determine the location of the bow shock,  
 34      the magnetopause and the neutral sheet **from** the spacecraft measurements and com-  
 35      pare their **locations to those predicted by the simulation**.

36      The GUMICS-4 **model** provides quite good results in the solar wind however its  
 37      accuracy is **worse** in the magnetosheath. The simulation results are not realistic in the  
 38      magnetosphere. The bow shock location is predicted well however the magnetopause lo-  
 39      cation is less accurate. The neutral sheet positions are located quite well thanks to the  
 40      special solar wind conditions. The reason for the **inaccuracy of the magnetopause**  
 41      **position and the parameters of the magnetosphere** is the missing inner magne-  
 42      tosphere model.

43      **1 Introduction**

44      One of the most cost-effective way to study the interaction of the solar wind **with**  
 45      planetary magnetospheres (or predict the conditions **in** near-Earth space) is **MODELING**  
 46      **THIS COMPLEX SYSTEM** using a global magnetohydrodynamic (MHD) code. In the past,  
 47      several [...] parallelized, effective, verified and validated codes were developed, which  
 48      are used and applied to forecast the cosmic environment of the Earth; such as the Lyon-  
 49      Fedder-Mobarry [LFM; *Lyon et al.*, 2004] code, **the Grid Agnostic MHD for Extended**  
 50      **Research Applications [GAMERA; *Zhang et al.*, 2019]**, the Open Geospace Gen-  
 51      eral Circulation Model [OpenGGCM; *Raeder et al.*, 2008], the Block-Adaptive-Tree-Solarwind-  
 52      Roe-Upwind-Scheme [BATS-R-US; *Powell et al.*, 1999; *Tóth et al.*, 2012]. In Europe only  
 53      three global MHD codes were developed: the Grand Unified Magnetosphere–Ionosphere  
 54      Coupling Simulation [GUMICS-4; *Janhunen et al.*, 2012], the Computational Object

55 Oriented Libraries for Fluid Dynamics [COOLFluiD; *Lani et al.*, 2012] and the 3D re-  
 56 sistive magnetohydrodynamic code Gorgon [*Chittenden et al.*, 2004; *Ciardi et al.*, 2007].  
 57 The COOLFluiD is a general-purpose plasma simulation tool. The Gorgon code was de-  
 58 veloped **to study** high energy, collisional plasma interactions and has been adapted to  
 59 simulate planetary magnetospheres and their interaction with the solar wind [*Mejnert-*  
 60 *sen et al.*, 2016, 2018]. **Neither Gorgon nor COOLfluid have an ionospheric solver.**  
 61 The GUMICS–4 **model** was developed to study the solar wind-terrestrial magnetosphere  
 62 interaction and its parallel version has not been available for the scientific community  
 63 **because it is still in development** (see Section 2.1). **Almost all of these codes are**  
 64 available at the Community Coordinated Modelling Center (CCMC; <http://ccmc.gsfc.nasa.gov/>)  
 65 hosted by the NASA Goddard Space Flight Center (GSFC) **or** the Virtual Space Weather  
 66 Modelling Centre (VSWMC; <http://swe.ssa.esa.int/web/guest/kul-cmpa-federated>; **re-**  
 67 **quires registration for the European Space Agency (ESA) Space Situational**  
 68 **Awareness (SSA) Space Weather (SWE) portal** hosted by the KU Leuven [*Poedts*  
 69 *et al.*, 2020]. **A** comparison of the simulation results **with** spacecraft and ground-based  
 70 measurements is necessary to understand the abilities and features of the developed tools.  
 71 **A** statistical study using long term global MHD runs for validation [...] of the codes  
 72 **seems is needed. Because** [...] providing long simulations **are** costly and time con-  
 73 suming [...], only a few studies **have been done, all for periods much less** than a  
 74 year.

75 *Guild et al.* [2008a,b] launched two months of LFM runs and compared the plasma  
 76 sheet properties in the simulated tail with the statistical properties of six years Geotail  
 77 magnetic field and plasma observations [*Kokubun et al.*, 1994; *Mukai et al.*, 1994]. The  
 78 LFM successfully reproduced the global features of the global plasma sheet in **a** statis-  
 79 tical sense. However, there were some differences. The sheet was too cold, too dense and  
 80 the bulk flow was faster than the observed plasma sheet [*Kokubun et al.*, 1994; *Mukai*  
 81 *et al.*, 1994]. The LFM overestimated the ionospheric transpolar potential. The trans-  
 82 polar potential correlated with the speed of the plasma sheet flows. **Equatorial maps of**  
 83 **density, thermal pressure, thermal energy and velocity** were compared. The LFM over-  
 84 estimated the plasma sheet density close to the Earth, the temperature by a factor of  
 85  $\sim 3$  **and** the global average flow speed by a factor of  $\sim 2$ . The LFM reproduced many of  
 86 the climatological features of the Geotail data set. The low-resolution model underes-  
 87 timated the occurrence of the fast earthward and tailward flows. Increasing the simu-

88 lation resolution resulted in the development of fast, busty flows. These flows influenced  
 89 the statistics and contributed to a better agreement between simulations and observa-  
 90 tions.

91 *Zhang et al.* [2011] [...] studied the statistics of magnetosphere-ionosphere (MI)  
 92 coupling using ***Guild et al.* [2008a]**'s LFM simulation above. The polar cap po-  
 93 tential and the field aligned currents (FAC), the downward Poynting flux and the vor-  
 94 ticity of the ionospheric convection were compared with observed statistical averages and  
 95 the Weimer05 empirical model [*Weimer*, 2005]. The comparisons showed that the LFM  
 96 model produced quite accurate average distributions of the Region 1 (R1) and Region  
 97 2 (R2) currents. The ionospheric R2 currents in the MHD simulation seemed to **orig-**  
 98 **inate** from the diamagnetic ring current. The average LFM R1 and R2 currents were  
 99 **small** compared with the values from the Weimer05 model. The average **Cross Polar Cap**  
 100 **Potential (CPCP)** was higher in the LFM simulation than the measurements of the Su-  
 101 perDARN and the Weimer05 model. The average convention pattern was quite symmet-  
 102 ric in the LFM simulation against the SuperDARN measurements and the Weimer05 model.  
 103 The SuperDARN measurements and the Weimer05 model had **a** dawn-dusk asymme-  
 104 try. In the LFM model, more Poynting flux flowed into the polar region ionosphere than  
 105 in the Weimer05 model. It was the consequence of the larger CPCP in the LFM sim-  
 106 ulation. The larger CPCP allowed **a** higher electric field in the polar region. The sta-  
 107 tistical dependence of the high-latitude convection patterns on Interplanetary Magnetic  
 108 Field (IMF) clock angle was similar to the SuperDARN measurements [*Sofko et al.*, 1995]  
 109 and the Weimer05 model. The average ionospheric field-aligned vorticity showed good  
 110 agreement on the dayside. However, the LFM model gave **a** larger nightside vorticity than  
 111 SuperDARN measurements because the Pedersen conductance on the night side iono-  
 112 sphere was too low.

113 *Wiltberger et al.* [2017] studied the structure of [...] high latitude field-aligned cur-  
 114 rent patterns using three resolutions of the LFM global MHD code and the Weimer05  
 115 empirical model [*Weimer*, 2005]. The studied period was a month long and contained  
 116 two high-speed streams. Generally, the patterns agreed well with results obtained from  
 117 the Weimer05 computing. As the resolution of the simulations increased, the currents be-  
 118 came more intense and narrow. The ratio of the Region 1 (R1), the Region 2 (R2) cur-  
 119 rents and the R1/R2 ratio increased when the simulation resolution increases. However,  
 120 both the R1 and R2 currents were smaller than the predictions of the Weimer05 model.

121 This effect led to a better agreement of the LFM simulation results with the Weimer 2005  
 122 model results. The CPCP pattern became concentrated in higher latitudes because of  
 123 the stronger R2 currents. The relationship of the CPCP and the R1 looked evident at  
 124 higher resolution of the simulation. The LFM simulation could have reproduced the sta-  
 125 tistical features of the field aligned current (FAC) patterns.

126 *Hajducek et al. [2017]* simulated **the month (January,2005)** using the Space Weather  
 127 Modelling Framework [SWMF; *Tóth et al.*, 2005] and the OMNI solar wind data (<https://omniweb.gsfc.nasa.gov/>)  
 128 as input. The simulations were **compiled** with and without **an** inner magnetosphere model  
 129 and using two different grid resolutions. The model was very good in predicting the **ring**  
 130 currents [...] [SYM-H; <http://wdc.kugi.kyoto-u.ac.jp/aeasy/asy.pdf>; *Iyemori*, 1990]. The  
 131  $K_p$  index (that measures the general magnetospheric convention and the auroral currents  
 132 [*Bartels et al.*, 1939; *Rostoker*, 1972; *Thomsen*, 2004]) was predicted well during storms  
 133 however the index was **overestimated** during quiet time periods. The AL index (that de-  
 134 scribes the westward electro jet of the surface magnetic field introduced by *Davis and*  
 135 *Sugiura* [1966]) was predicted reasonably well **on** average. However the model reached  
 136 the highest negative AL value less often **it was reached in the** observations because the  
 137 model captured the structure of the auroral zone currents poorly. The overpredicting of  
 138  $K_p$  index during quiet times might have had the same reason because that index was also  
 139 sensitive **to** auroral zone dynamics. The SWMF usually over predicted the CPCP. These  
 140 results were not sensitive to grid **resolutions, with the except of** the AL index, **whitch**  
 141 reached the highest negative value more often when the grid resolution was higher. Switch-  
 142 ing off of the inner magnetosphere model had **a negative effect on** the accuracy of all  
 143 quantities mentioned above, except the CPCP.

144 In this paper, the Cluster SC3 measurements are compared directly to a previously  
 145 made 1-year long GUMICS–4 simulation in the solar wind, magnetosheath and the mag-  
 146 netosphere along the Cluster SC3 orbit saved from the simulation results and measured  
 147 by the spacecraft [*Facskó et al.*, 2016]. In this paper these parameters, namely the  $B_z$ ,  
 148 **the north/south component of the magnetic field in GSE coordinates**, the solar  
 149 wind velocity GSE X component ( $V_x$ ) and the solar wind density  $n$  are compared to the  
 150 Cluster SC3 measurements as well as the location of the bow shock, magnetopause and  
 151 the neutral sheet. These parameters are selected because [...]  $B_z$  controls the magne-  
 152 tosphere, [...]  $V_x$  is the main **component of the** solar wind velocity [...] and [...]  
 153  $n$  is the ion plasma momentum that is the easiest to calculate; furthermore more instru-

154       ments could determine it (see Section 2.2). The structure of this paper is as follows. Sec-  
 155       tion 2 describes the GUMICS–4 code, the 1-year simulation and the considered mea-  
 156       surements of the Cluster space mission. Section 3 gives comparisons between the sim-  
 157       ulations and observations. Results of the comparison are discussed in Section 4. Finally,  
 158       Section 5 contains the conclusions.

## 159       2 The GUMICS–4 products and Cluster measurements

160       Here we use two [...] very different [...] time series. The first type is derived from  
 161       a previously 1-year run of the GUMICS–4 simulation [Facskó et al., 2016]. The sec-  
 162       ond time series were measured by the magnetometer, ion plasma and electric field in-  
 163       struments of the Cluster reference spacecraft.

### 164       2.1 The GUMICS–4 code

165       The GUMICS–4 has two coupled simulation domains, the magnetospheric domain  
 166       outside of  $3.7 R_E$  radius sphere around the Earth and a coupled ionosphere module con-  
 167       taining a 3D electron density model for the ionosphere. The GUMICS–4 is not a par-  
 168       allel code however it has been extensively used for studying the energy propagation pro-  
 169       cesses from the solar wind to the magnetosphere through the magnetopause and other  
 170       features [Janhunen et al., 2012, see the references therein]. The code has also been ap-  
 171       plied to study forced reconnection in the tail [Vörös et al., 2014]. Recently, several  
 172       hundred synthetic two hours duration GUMICS–4 simulation runs were made to com-  
 173       pare the simulation results to empirical formulas [Gordeev et al., 2013]. The agreement  
 174       was quite good in general, but the diameter of the magnetopause [...] in the simula-  
 175       tion deviated significantly from observations in the tail. The [...] GUMICS–4 sim-  
 176       ulation magnetotail was smaller than what the spacecraft observed and measured. A  
 177       1-year long simulation was made using the GUMICS–4 code [Facskó et al., 2016]. Ju-  
 178       usola et al. [2014] compared the ionospheric currents, fields and the [...] CPCP in the  
 179       simulation to observations from the Super Dual Auroral Radar Network (SuperDARN)  
 180       radars [Greenwald et al., 1995] and CHAMP spacecraft [Reigber et al., 2002] field aligned  
 181       currents (FAC) measurements [Juusola et al., 2007; Ritter et al., 2004]. The agreement  
 182       was good for the seasonal variation of the CPCP, however, the FAC and other currents  
 183       could not be reproduced properly. The possible cause of this poor agreement could be  
 184       the lack of an inner magnetosphere model incorporating the physics in this region.

This hypothesis is supported by the result of Haiducek *et al.* [2017]. Haiducek *et al.* simulated only a month-long period using a different spatial resolution and [...] tested the code with the inner magnetosphere model of the SWMF switched off for a special run. This run without an inner magnetosphere model made it clear that only the CPCP parameter of the simulation agreed quite well with the measurements. This fact explained why the agreement between the Cluster SC3 and the GUMICS-4 simulations was so good as described by Lakka *et al.* [2018a,b] based on the CPCP in GUMICS-4 simulations. Kallio and Facskó [2015] determined plasma and magnetic field parameters along the lunar orbit from the Facskó *et al.* [2016]'s global MHD simulations. The [...] parameters differed significantly in the geotail indicating a need for future studies. Facskó *et al.* [2016] determined the footprint of [...] Cluster SC3 using the 1-year simulation and the Tsyganenko T96 empirical model [Tsyganenko, 1995]. The code seemed to react slower to the dynamic changes of the solar wind pressure than the empirical model. The agreement of the footprint was better in the Northern Hemisphere. The GUMICS-4 tail was shorter in the simulations than the observations. Finally, the Y component of the interplanetary magnetic field twisted the simulated tail hence the agreement of the empirical and computational footprints was worse when such solar wind conditions prevailed.

A 1-year global MHD simulation was produced with the GUMICS-4 code using the OMNI solar wind data from January 29, 2002 to February 2, 2003 as input [Facskó *et al.*, 2016]. The creation and analysis of the simulation was based on a workpackage of the European Cluster Assimilation Technology (ECLAT) project ([https://cordis.europa.eu/result/rcn/165813\\_en.html](https://cordis.europa.eu/result/rcn/165813_en.html)). The GUMICS-4 was a single core system [Janhunen *et al.*, 2012] hence the 1-year simulation was made in 1860 independent runs. This interval covered 155 Cluster SC3 orbits and each orbit lasted 57 hours. The supercomputer had 12 CPUs on each node hence the 57 hours were divided into 4.7 hours simulation time with one hour initialisation period. Each sub-interval used its own individual average Geocentric Solar Ecliptic (GSE) IMF magnetic field X component  $B_x$  component and dipole tilt angle. All data gaps of the input file were filled using interpolation. If the data gap of the input file was at the beginning (or the end) of the interval then the first (or last) good data from the input file was used to fill the gap. The initialisation of each simulation run was made using constant values. These values were the first valid data of the input file repeated 60 times (60 minutes) in the input file of the sub-interval. The

simulation results were saved [...] every five minutes. Various simulation parameters, for example, the density, particle density, temperature, magnetic field, solar wind velocity (29 different quantities) were saved from the simulation results along the Cluster reference spacecraft's **orbit** in the GSE coordinates. [...]

## 222      2.2 The Cluster SC3 measurements

The Cluster-II spacecraft of the European Space Agency (ESA) were launched in 2000 and study the geospace [...] [Credland *et al.*, 1997; Escoubet *et al.*, 2001]. The four spacecraft form a tetrahedron **in space** however here we use only the measurements of the reference spacecraft, [...] Cluster SC3. The spacecraft were stabilised [...] and their period is  $\sim 4$  s. Hence, the **intrinsic time** resolution of the plasma instruments is 4 s and we use 4 s averaged magnetic field data. The **highest** resolution of the Cluster FluxGate Magnetometer (FGM) magnetic field instrument is 27 Hz [Balogh *et al.*, 1997, 2001]. The ion plasma data **are** provided by the Cluster Ion Spectrometry (CIS) Hot Ion Analyser (HIA) sub-instrument [Reme *et al.*, 1997; Rème *et al.*, 2001]. The CIS HIA instrument is calibrated using the Waves of High frequency Sounder for Probing the Electron density by Relaxation (WHISPER) wave instrument onboard Cluster [Décréau *et al.*, 2001; Trotignon *et al.*, 2010; Blagau *et al.*, 2013, 2014]. The results of these calibrations **can appear** as sudden non-physical jumps in the CIS HIA data. The CIS HIA had different modes to measure in the solar wind and the magnetosphere. When the instrument switched from **one** mode to another mode it appeared as a non-physical **jumps also appear** in the **measurements** [...]. These features **impair** the accuracy of [...] data **analyses**.

We protect our results from these non-physical jumps [...] using a density determination based on different principles. We use the spacecraft potential of the Electric Field and Wave Experiment [EFW ; Gustafsson *et al.*, 1997, 2001] to determine the electron density. This quantity can be calculated using the empirical density formula

$$n_{EFW} = 200(V_{sc})^{-1.85}, \quad (1)$$

where  $n_{EFW}$  is the calculated density and  $V_{sc}$  is the Cluster EFW spacecraft potential [Trotignon *et al.*, 2010, 2011]. The EFW and the WHISPER were used for the calibration of the CIS HIA and the Plasma Electron and Current Experiment [PEACE; Johnstone *et al.*, 1997; Fazakerley *et al.*, 2010a,b]. Both instruments were still working on-

248 board all Cluster spacecraft. Their stable operation reduced the number of data **gaps**,  
 249 and it also made the data analysis easier.

### 250 3 Comparison of measurements to simulation

251 The [...] parameters **saved** from the GUMICS–4 simulations and the Cluster SC3  
 252 magnetic field, solar wind velocity and density measurements are compared in **differ-**  
 253 **ent regions, namely** the solar wind, magnetosheath and magnetosphere using cross  
 254 correlation calculation. The **temporal** resolution of the simulated Cluster orbit data is  
 255 mostly five minutes because the **results of the simulations** are saved [...] every five min-  
 256 utes [Fazekas et al., 2016]. However, the time difference between points **can** be more than  
 257 five minutes at the boundary of the subintervals, because the length of **the** simulation  
 258 intervals is determined in minutes. To facilitate analysis of the simulation results, all sim-  
 259 ulation data were interpolated to one minute resolution. This method does not provide  
 260 extra information to the cross correlation calculation. The data gaps are eliminated us-  
 261 ing **linear** interpolation [...] and extrapolation when the gap is at the start or the end  
 262 of the selected interval. The spin resolution (4 s) of Cluster SC3 magnetic field measure-  
 263 ments is averaged over one minute around ( $\pm 30$  s) the time stamps of the saved data.

264 For the correlation calculation, intervals are selected carefully in the solar wind (see  
 265 **Section 3.1**), the magnetosheath (see **Section 3.2**), the dayside and the night side mag-  
 266 netosphere (see **Section 3.3**). In these intervals, the parameters did not vary a lot and  
 267 **we require** neither [...] Cluster nor the virtual probe **to cross** any boundaries. To  
 268 compare [...] the  $B_z$  magnetic field,  $V_x$  solar wind speed and the  $n_{CIS}$  and the  $n_{EFW}$   
 269 curves we [...] cross **correlate** selected intervals. [...] We carefully examine **such** cases  
 270 and remove [...] intervals **which are too short for the  $\pm 60$  minutes correlation calcula-**  
**tion** (shorter than four hours) [...] and large data gaps from the correlation calcula-  
 271 tion. [...] Those intervals are also neglected where the plasma instrument has a cali-  
 272 bration error or a **change in its recording mode as it moves from the** magnetosphere to  
 273 solar wind (for example). The electron density is also calculated using [...] Equation 1  
 274 and [...] correlated [...]. We want to avoid **the** calibration errors and sudden non-  
 275 physical jumps mentioned previously. The **correlation results for the density de-**  
 276 **rived from the electric field potential** results do not differ significantly **from those**  
 277 **for the top hat plasma instrument**, however the  $n_{EFW}$  does not have any mode change  
 278 and it is applicable in the magnetosphere too (against the CIS HIA instrument).

280        **3.1 Solar wind**

We use OMNI IMF and solar wind velocity, density and temperature data as input to the simulation. There is a reason why we compare parameters in the solar wind region in the simulation and the measurements. The IMF X component cannot be given to the GUMICS–4 as input [Janhunen *et al.*, 2012; Fazekó *et al.*, 2016]. However, the magnetic field of the solar wind has an X component in the simulations. Additionally, the solar wind structure might change from the simulation domain boundary at  $+32 R_E$  to the sub-solar point of the terrestrial bow shock where all OMNI data is shifted. Almost the same solar wind time intervals are used as in [...] Table 1 of Fazekó *et al.* [2016]. The number of these intervals is small because [...] Cluster fleet instruments were calibrated in 2002, just after launch (Table 1). Hence we do not have a satisfactory ion plasma data coverage for this year. Additionally, to improve the accuracy of the correlation calculation (see below) we delete the intervals that were too short (shorter than five hours) or the CIS HIA instrument changed its mode. The Cluster fleet is located in the solar wind only from December to May and only for a couple of hours during each orbit near [...] apogee. We double check whether the Cluster SC3 stays in the solar wind in both the simulation and reality. We also check the omnidirectional CIS HIA ion spectra on the Cluster Science Archive (CSA; <https://www.cosmos.esa.int/web/csa/csds-quicklook-plots>). The spectra must contain one narrow band in the solar wind region. Hence 17 intervals are left in the solar wind to study (Figure 1).

The selected intervals occur for quiet solar wind conditions (Figure 2). The GUMICS–4 simulation results have five minutes resolution and the Cluster SC3 measurements have one minute resolution (Figure 3). The measurements vary significantly. In spite of the quiet conditions the solar wind density often changes and deviates from the simulation. [...] Figure 4c shows that both densities deviate significantly. The CIS HIA density deviation is larger as [...] expected given the complexity and the large number of working modes of the CIS instrument. The magnetic field and the solar wind velocity fit better. [...] Figure 5a shows that the correlation of the magnetic fields is very good; furthermore on Figure 5c, 5e, 5f the correlation of the solar wind velocity and density is excellent (Table 1). The time shift on Figure 5b, Figure 5d, Figure 5f is about five minutes for the magnetic field and the CIS data. On Figure 5h for the EFW data the time shift is less stable. It is not as well determined as in case of the other parameters.

312        **3.2 Magnetosheath**

313        The Cluster SC3 spent only a little time in the solar wind from December, 2002  
 314        to May, 2003. However, the [...] spacecraft **enters** the magnetosheath each orbit (Figure 6). We selected intervals when the value of the magnetic field is around 25 nT. The  
 315        field should be fluctuating because of the turbulent **deflected** flow of the **shocked** so-  
 316        lar wind [...] the **temperature should be greater than that in the solar wind** [...].  
 317        The **velocity should decrease to values ranging from** 100-300 km/s. The density  
 318        of the plasma **should increase** and reached **values of** 10-20 cm<sup>-3</sup>. The narrow band  
 319        on the omnidirectional CIS HIA ion spectra from the CSA (<https://www.cosmos.esa.int/web/csa/csds-quicklook-plots>) **widens from the solar wind to the magnetosheath**. 15–30 minutes  
 320        **from each bow shock** crossing we considered the Cluster SC3 to **have entered** into  
 321        the magnetosheath. At the inner **magnetopause** boundary **of the magnetopause** the  
 322        flow speed [...] and the density **drop**. The magnetic field **strength increases** and the  
 323        **magnetic field becomes** less turbulent than in the magnetosheath. The wide band on  
 324        the the omnidirectional CIS HIA ion spectra disappears. 15-30 minutes before the ap-  
 325        pearance of these indicators of the magnetopause crossing our intervals end. All inter-  
 326        vals contain large data gaps, non-physical jump **in** instrument modes [...] or **lasting**  
 327        **less** than four hour are removed. Hence 74 intervals considered in our final selection (Ta-  
 328        ble 2).

331        All intervals have quiet upstream (or input) solar wind conditions (Figure 7). **In spite**  
 332        **of** our selected [...] magnetic field and [...] plasma parameters and the calculated em-  
 333        pirical density **indicate that they** vary significantly stronger than in the solar wind in-  
 334        tervals (Figure 8). The deviation **between** the simulated and the observed data is **also**  
 335        larger in this region [...] . The **scatter** plots of the magnetic field, plasma flow speed  
 336        and the densities **show that these parameters agree well, but with greater vari-**  
 337        **ation** than the **scatter** plots **for** the solar wind (Figure 9a, 9b, 9c). The correlation of  
 338        the simulated and the observed data is good for the magnetic field (Figure 10a), very  
 339        good for the ion plasma moments and the calculated density (Figure 10c, 10e, 10g). The  
 340        timeshift of the magnetic field is within five minutes mostly (Figure 10b) however the  
 341        timeshift of the ion plasma moments is scattered (Figure 10d, 10f). The timeshift of the  
 342        calculated EFW density seems to be more **stable** (Figure 10h). Generally, the GUMICS-4  
 343        is less accurate in the magnetosheath **than in the solar wind**. **The modelled mag-**  
 344        **netic field is closer to the observations than the modelled plasma parameters**

345      **are.** The calculated empirical EFW density ( $n_{EFW}$ ) fits better than the CIS HIA den-  
 346      sity ( $n_{CIS}$ ).

347      **3.3 Magnetosphere**

348      To select intervals in the magnetosphere we looked for the CIS HIA **omnidirectional**  
 349      ion flux **spectrum**. Where the band of the hot magnetosheath ion population (dis)appeared,  
 350      the magnetosphere started/finished. The **plasma** density **decreases toward** zero, the  
 351      magnetic field **strength is large**. We left 15–30 min after/before the magnetopause trans-  
 352      sition to **identify** magnetosphere **intervals**. This way we found 132 intervals in the mag-  
 353      netosphere (Table 3) using Cluster SC3 measurements. [...] Cluster SC3 spends con-  
 354      siderable time in the magnetosphere (Figure 11).

355      Here we show neither any correlation calculation nor comparison plot. In the mag-  
 356      netosphere the GUMICS–4 does not work well. Neither the magnetic field nor the plasma  
 357      moments nor the  $N_{EFW}$  fit well. The solar wind velocity does not reach zero in the sim-  
 358      ulation. Instead, the solar wind enters to the night side magnetosphere. The solar wind  
 359      CIS HIA ion plasma density and the calculated density from spacecraft potential increase  
 360      closer to the Earth (plasmasphere). The GUMICS–4 density is low there. We calculated  
 361      the dipole field in GSE using Tsyganenko geotool box [Tsyganenko, 1995] and substracted  
 362      from both the observed and the simulated magnetic field  $B_z$  data. The correlation of these  
 363      corrected magnetic field measurements and simulations is very low too.

364      **3.4 Bow shock, magnetopause, neutral sheet**

365      **77** intervals are selected when [...] Cluster SC3 crossed the terrestrial bow shock  
 366      once or multiple times (**Table 6**). When the spacecraft crosses the bow shock **inbound**  
 367      the magnitude of the magnetic field and the solar wind density increases **by a factor**  
 368      **of 4–5 times** (from 5 nT or  $5 \text{ cm}^{-3}$ , respectively), the solar wind speed drops from 400–  
 369      600 km/s to 100–300 km/s; furthermore the narrow band on the omnidirectional Clus-  
 370      ter CIS HIA ion spectra [...] widens. The Cluster measurements are 1-min averaged  
 371      **whereas** the GUMICS–4 simulations have 5–min resolution. Hence all bow shock tran-  
 372      sitions of the virtual spacecraft are slower and smoother. Additionally, the multiple bow  
 373      shock transitions are not visible in the GUMICS simulations. The code reacts slowly for  
 374      such sudden changes. The magnetic signatures fit better than the calculated plasma mo-

375       ments. The jump of the ion plasma parameters and the derived Cluster EFW density  
 376       of the simulations are shifted to the measurements. Generally, the density and the ve-  
 377       locity of the simulations seem to be less accurate than the magnetic field of the simu-  
 378       lations.

379       **54** intervals are selected around magnetopause crossings [...] (**Table 7**). When  
 380       the spacecraft crosses the magnetopause **inbound** the magnitude of the magnetic field  
 381       increases, the solar wind speed drops from 100–300 km/s to zero, the plasma density be-  
 382       comes zero; furthermore the wide band on the omnidirectional Cluster CIS HIA ion spec-  
 383       tra disappears. [...] The location of the magnetopause is well determined by the Clus-  
 384       ter SC3 measurements. However, it is very difficult to identify the magnetopause cross-  
 385       ings in the simulation data. [...] The magnetopause crossings very often cannot be seen  
 386       in the simulations. Or when the magnetopause crossings are clearly identified in both  
 387       simulations and spacecraft measurements the events are shifted. The accuracy of the model  
 388       is lower for the dayside magnetopause locations.

389       Nine intervals are chosen around Cluster SC3 neutral sheet crossings (Figure 12;  
 390       Table 8). The neutral **sheet** locations **are** determined using the results of the Bound-  
 391       ary Layer Identification Code (BLIC) Project [*Facskó et al.*, in preparation]. The BLIC  
 392       code determines the neutral sheet crossing Cluster FGM magnetic field measurements  
 393       using *Wang and Xu* [1994]’s method. When the solar wind speed is almost zero; further-  
 394       more the CIS HIA density and the EFW calculated density are almost zero too; finally  
 395       the GSE Z component of the magnetic field changes is a sign of the code indicated neu-  
 396       tral sheet crossing (Figure 20; red and blue curves). Surprisingly the neutral sheet cross-  
 397       ings are visible very well in the GUMICS simulations (Figure 20; black curves). For five  
 398       events (from nine Cluster SC3 crossings) the GUMICS–4 also provides similar smoothed  
 399       parameters and change of sign of the  $B_z$  component. This is a **outstanding** result be-  
 400       cause the tail in the GUMICS–4 simulations is significantly smaller than the observed  
 401       reality [*Gordeev et al.*, 2013; *Facskó et al.*, 2016]; furthermore the solar wind enters the  
 402       tail in MHD simulations generally [*Kallio and Facskó*, 2015].

## 4 Discussion

404       The agreement of [...]  $B_z$ ,  $V_x$  and  $n_{EFW}$  **in the solar wind** with the similar GU-  
 405       MICS simulation **predictions** is very good (Figure 4a, 4b, 4c, blue). The agreement of

[...]  $n_{CIS}$  is worse (Figure 4c, red). It was expected because the  $n_{EFW}$  depends on the spacecraft potential provided by the EFW instrument. However, the CIS instrument has many modes for measuring the plasma parameters and it needs **periodic** calibration too. The correlation of the solar wind  $V_x$ ,  $n_{CIS}$  and  $n_{EFW}$  with the similar GUMICS simulation parameters is greater than 0.9 (Figure 5c, 5e, 5g). The correlation of the  $B_z$  is also greater than 0.8 (Figure 5a). [...] The **upstream boundary** of the GUMICS–4 code **lies** at  $32 R_E$  [Janhunen et al., 2012], the nose of the terrestrial bow shock is at about  $20 R_E$ . If the solar wind speed is 400 km/s, then this spatial distance means less than **a** 5 minutes delay, so it should not be visible **in the time delays from the cross correlations**. 80% of the intervals support this theory but 20 % **do** not. In these cases, the one-minute resolution  $B_z$ ,  $n_{CIS}$  or the  $n_{EFW}$  parameters have a sudden jump or variation that the simulation cannot follow, or the resolution of the simulation data (5 minutes) is too small to see these variations. Therefore, the correlation calculation is not accurate in these cases. Previously the OMNI data was compared to the Cluster data and the Cluster measurements were compared to the GUMICS–4 [Facskó et al., 2016]. The comparison suggests that the GUMICS–4 results should be similar **for** the OMNI data. Furthermore, we calculate correlation functions in the solar wind, where there is no significant perturbation of the input parameters in the simulation box. Therefore, we get **the** expected result after comparing the two different correlation calculations.

In the magnetosheath we get worse agreement with the GUMICS simulation data (Figure 9a, 9b, 9c). **While the parameters are correlated, the scatter is greater.** The general reason **for** this larger uncertainty seems to be [...] **that the magnetosheath is turbulent.** This phenomena explains the higher variations of the  $B_z$  magnetic field on Figure 9a. The solar wind  $V_x$ ,  $n_{CIS}$  and  $n_{EFW}$  agree better than the magnetic field component (Figure 9b, 9c). Here there is no deviation between the densities derived in different ways ( $n_{CIS}$  and  $n_{EFW}$ ) on Figure 9c. Figure 10 seems to contradict these statements above. The larger uncertainty of the  $B_z$  is visible on Figure 10a. However, that correlation is still good on Figure 10b. The other parameters have larger ( $> 0.9$ ) correlation **in** Figure 10c, 10e, 10g. However, the time shifts **in** Figure 10d, 10f, 10h seem to be worse. Actually here the time shifts are worse because the shape of the time series in the magnetosheath looks very **smooth and similar hence there is not enough points to get a sharp and large maximum correlation as the function of timeshift.** **The difference between the minimum and the maximum of the correlation**

439    is small comparing with the uncertainty of the calculation. The maximum,  
 440    the timeshift could be anywhere and the shape of the correlation vs. timeshift  
 441    function is often neither symmetric nor has only one local maximum. Hence,  
 442    the correlation calculation provides larger time shifts for the ion plasma parameters and  
 443    the  $n_{EFW}$ .

444    In the magnetosphere the GUMICS-4 does not work well. [...] GUMICS-4 uses  
 445    a tilted dipole to describe the terrestrial magnetic field [Janhunen *et al.*, 2012]. After re-  
 446    moving the magnetic dipole from the magnetic field measurements of the Cluster SC3  
 447    and the simulation we get very low correlations and unacceptable time shifts (not shown).  
 448    [...] The tilted dipole is an insufficient description **of the inner magnetospheric mag-**  
 449    **netic field.** [...] The plasma **moments** and the  $n_{EFW}$  do not fit either. The MHD ap-  
 450    proach lost its validity in the inner magnetosphere domain therefore [...]  $V_x$  and [...]  
 451     $n$  **in** the simulations do not agree **with**  $V_x$ , [...]  $n_{CIS}$  and the  $n_{EFW}$  measured by the  
 452    Cluster SC3. Within the  $3.7 R_E$  domain **ring current physics must be added**, as  
 453    **it has been** in other global MHD codes [Lyon *et al.*, 2004; Raeder *et al.*, 2008; Powell  
 454    *et al.*, 1999; Tóth *et al.*, 2012]. This result explains the limited accuracy of the cross po-  
 455    lar cap potential (CPCP) and geomagnetic indices of the GUMICS simulations [Juusola  
 456    *et al.*, 2014]. The CPCP [...] GUMICS **agrees well with** spacecraft measurements there-  
 457    fore this quantity could be used for [...] simulation studies [Lakka *et al.*, 2018a]. Haiducek  
 458    *et al.* [2017] also [...] **compared** [...] geomagnetic indices and the CPCP. The Space  
 459    Weather Modelling Framework (SWMF) was tested. When the inner magnetosphere model  
 460    was switched off in the simulation only the comparison of the simulated and observed  
 461    CPCP was good. Therefore, the reason of the discrepancy of the geomagnetic indices  
 462    in the GUMICS simulations must be the missing inner magnetosphere model.

463    The reason of why simulation results and [...] measurements disagree  
 464    could be the code or the bad input parameters. During the 1-year run the  
 465    distributions of the OMNI solar wind magnetic field  $B_x$ ,  $B_y$ ,  $B_z$  components  
 466    (Figure 13a, 13b, 13c); solar wind velocity  $V_x$ ,  $V_y$ ,  $V_z$  components (Figure 13d, 13e, 13f)  
 467    and the solar wind  $P$  dynamic pressure are calculated (Figure 13g) from Jan-  
 468    uary 29, 2002 to February 2, 2003 in GSE reference frame. The intervals when  
 469    the GUMICS-4 simulations and the Cluster SC3 measurements disagreed  
 470    are collected for intervals in the solar wind (Table 4) and the magnetosheath  
 471    (Table 5). The averaged shifted OMNI parameters of the poorly agreeing in-

472    tervals from the Tables 4 and 5 are saved. The distributions of the OMNI  
 473    parameters belonging to the bad simulation results are calculated for the so-  
 474    lar wind region (Figure 14, 15 and 16) and in the magnetosheath (Figure 17, 18 and 19).

- 475    1. In the solar wind the distributions of the OMNI  $B_x$ ,  $B_y$  and  $B_z$  can be  
 476    compared in Figure 13a and Figure 14a, 14d, 14g, 14j; Figure 13b and  
 477    Figure 14b, 14e, 14h, 14k; furthermore in Figure 13c and Figure 14c, 14f, 14i, 14l.  
 478    (a) When the  $B_z$  disagrees in simulations and measurements in Figure 14a, 14b, 14c  
 479    the distributions of the OMNI  $B_x$ ,  $B_y$  and  $B_z$  are not similar to the  
 480    distributions of the OMNI  $B_x$ ,  $B_y$  and  $B_z$  in Figure 13a, 13b and 13c.  
 481    The reason of these strange spikes is that there is only one poorly cor-  
 482    related interval for the  $B_z$  in the solar wind according to Table 4.  
 483    (b) When the  $V_x$  disagrees in simulations and measurements in Figure 14d, 14e, 14f  
 484    the distributions of the OMNI  $B_x$ ,  $B_y$  and  $B_z$  are similar to the dis-  
 485    tributions of the OMNI  $B_x$ ,  $B_y$  and  $B_z$  in Figure 13a, 13b and 13c.  
 486    The distributions do not agree perfectly because in Table 4 the num-  
 487    ber of the poorly correlated intervals is only six for the  $V_x$  component.  
 488    (c) When the  $n_{CIS}$  disagrees in simulations and measurements in Figure 14g, 14h, 14i  
 489    the distributions of the OMNI  $B_x$ ,  $B_y$  and  $B_z$  are similar to the dis-  
 490    tributions of the OMNI  $B_x$ ,  $B_y$  and  $B_z$  in Figure 13a, 13b and 13c.  
 491    The distributions do not agree perfectly because in Table 4 the num-  
 492    ber of the poorly correlated intervals is only 12 for the  $n_{CIS}$ .  
 493    (d) When the  $n_{EFW}$  disagrees in Figure 14j, 14k, 14l the distributions of  
 494    the OMNI  $B_x$ ,  $B_y$  and  $B_z$  are similar to the distributions of the OMNI  
 495     $B_x$ ,  $B_y$  and  $B_z$  in Figure 13a, 13b and 13c. The distributions do not  
 496    agree perfectly because in Table 4 the number of the poorly corre-  
 497    lated intervals is only nine for  $n_{EFW}$ .

498    The values of the OMNI  $B_x$ ,  $B_y$  and  $B_z$  are not peculiar in the solar wind.

- 499    2. In the solar wind the distributions of the OMNI  $V_x$ ,  $V_y$  and  $V_z$  can be  
 500    compared in Figure 13d and Figure 15a, 15d, 15g, 15j; Figure 13e and  
 501    Figure 15b, 15e, 15h, 15k; furthermore in Figure 13f and Figure 15c, 15f, 15i, 15l.  
 502    (a) When the  $B_z$  disagrees in Figure 15a, 15b, 15c the distributions of  
 503    the OMNI  $V_x$ ,  $V_y$  and  $V_z$  are not similar to the distributions of the OMNI

504       $V_x$ ,  $V_y$  and  $V_z$  in Figure 13d, 13e and 13f. The reason of these strange  
 505      spikes is that there is only one poorly correlated interval for the  $B_z$   
 506      in the solar wind according to Table 4.

- 507      (b) When the  $V_x$  disagrees in simulations and measurements in Figure 15d, 15e, 15f  
 508      the distributions of the OMNI  $V_x$ ,  $V_y$  and  $V_z$  are similar to the dis-  
 509      tributions of the OMNI  $V_x$ ,  $V_y$  and  $V_z$  in Figure 13d, 13e and 13f. The  
 510      distributions do not agree perfectly because in Table 4 the number  
 511      of the poorly correlated intervals is only six for the  $V_x$  component.
- 512      (c) When the  $n_{CIS}$  disagrees in Figure 15g, 15h, 15i the distributions of  
 513      the OMNI  $V_x$ ,  $V_y$  and  $V_z$  are similar to the distributions of the OMNI  
 514       $V_x$ ,  $V_y$  and  $V_z$  in Figure 13d, 13e and 13f. The distributions do not agree  
 515      perfectly because in Table 4 the number of the poorly correlated in-  
 516      tervals is only 12 for the  $n_{CIS}$ .
- 517      (d) When the  $n_{EFW}$  disagrees in simulations and measurements in Fig-  
 518      ure 15j, 15k, 15l the distributions of the OMNI  $V_x$ ,  $V_y$  and  $V_z$  are sim-  
 519      ilar to the distributions of the OMNI  $V_x$ ,  $V_y$  and  $V_z$  in Figure 13d, 13e  
 520      and 13f. The distributions do not agree perfectly because in Table 4  
 521      the number of the poorly correlated intervals is only nine for the  $n_{EFW}$ .

522      The values of the OMNI  $V_x$ ,  $V_y$  and  $V_z$  are not peculiar in the solar wind.

523      3. In the solar wind the distributions of the OMNI  $P$  can be compared in  
 524      Figure 13g and Figure 16a, 16b, 16c, 16d.

- 525      (a) When the  $B_z$  disagrees in Figure 16a the distribution of the OMNI  
 526       $P$  is not similar to the distribution of the OMNI  $P$  in Figure 13g. The  
 527      reason of these strange spike is that there is only one poorly corre-  
 528      lated interval for the  $B_z$  in the solar wind according to Table 4.
- 529      (b) When the  $V_x$  disagrees in simulations and measurements in Figure 16b  
 530      the distribution of the OMNI  $P$  is similar to the distributions of the  
 531      OMNI  $P$  in Figure 13g. The distributions do not agree perfectly be-  
 532      cause in Table 4 the number of the poorly correlated intervals is only  
 533      six  $V_x$  component.
- 534      (c) When the  $n_{CIS}$  disagrees in simulations and measurements in Figure 16c  
 535      the distribution of the OMNI  $P$  is similar to the distributions of the

536 OMNI  $P$  in Figure 13g. The distributions do not agree perfectly be-  
 537 cause in Table 4 the number of the poorly correlated intervals is only  
 538 12 for the  $n_{CIS}$ .

539 (d) When the  $n_{EFW}$  disagrees in simulations and measurements in Fig-  
 540 ure 16d the distribution of the OMNI  $P$  is similar to the distributions  
 541 of the OMNI  $P$  in Figure 13g. The distributions do not agree per-  
 542 fectly because in Table 4 the number of the poorly correlated inter-  
 543 vals is only nine for the  $n_{EFW}$ .

544 The values of the OMNI  $P$  are not peculiar in the solar wind.

545 4. In the magnetosheath the distributions of the OMNI  $B_x$ ,  $B_y$  and  $B_z$  can  
 546 be compared in Figure 13a and Figure 17a, 17d, 17g, 17j; Figure 13b  
 547 and Figure 17b, 17e, 17h, 17k; furthermore in Figure 13c and Figure 17c, 17f, 17i, 17l.

- 548 (a) When the  $B_z$  disagrees in simulations and measurements in Figure 17a, 17b, 17c  
 549 the distributions of the OMNI  $B_x$ ,  $B_y$  and  $B_z$  are similar to the dis-  
 550 tributions of the OMNI  $B_x$ ,  $B_y$  and  $B_z$  in Figure 13a, 13b and 13c.  
 551 (b) When the  $V_x$  disagrees in simulations and measurements in Figure 17d, 17e, 17f  
 552 the distributions of the OMNI  $B_x$ ,  $B_y$  and  $B_z$  are similar to the dis-  
 553 tributions of the OMNI  $B_x$ ,  $B_y$  and  $B_z$  in Figure 13a, 13b and 13c.  
 554 (c) When the  $n_{CIS}$  disagrees in simulations and measurements in Figure 17g, 17h, 17i  
 555 the distributions of the OMNI  $B_x$ ,  $B_y$  and  $B_z$  are similar to the dis-  
 556 tributions of the OMNI  $B_x$ ,  $B_y$  and  $B_z$  in Figure 13a, 13b and 13c.  
 557 (d) When the  $n_{EFW}$  disagrees in Figure 17j, 17k, 17l the distributions of  
 558 the OMNI  $B_x$ ,  $B_y$  and  $B_z$  are similar to the distributions of the OMNI  
 559  $B_x$ ,  $B_y$  and  $B_z$  in Figure 13a, 13b and 13c.

560 The distributions agree quite well because in Table 5 the number of the  
 561 poorly correlated intervals 18, 50, 33 and 30 for the  $B_z$ , the  $V_x$ , the  $n_{CIS}$   
 562 and  $n_{CIS}$  components, respectively. The number of cases are higher and  
 563 the values of the OMNI  $B_x$ ,  $B_y$  and  $B_z$  are not peculiar in the magne-  
 564 tosheath.

565 5. In the magnetosheath the distributions of the OMNI  $V_x$ ,  $V_y$  and  $V_z$  can  
 566 be compared in Figure 13d and Figure 18a, 18d, 18g, 18j; Figure 13e  
 567 and Figure 18b, 18e, 18h, 18k; furthermore in Figure 13f and Figure 18c, 18f, 18i, 18l.

- 568        (a) When the  $B_z$  disagrees in Figure 18a, 18b, 18c the distributions of  
 569        the OMNI  $V_x$ ,  $V_y$  and  $V_z$  are similar to the distributions of the OMNI  
 570         $V_x$ ,  $V_y$  and  $V_z$  in Figure 13d, 13e and 13f.
- 571        (b) When the  $V_x$  disagrees in simulations and measurements in Figure 18d, 18e, 18f  
 572        the distributions of the OMNI  $V_x$ ,  $V_y$  and  $V_z$  are similar to the dis-  
 573        tributions of the OMNI  $V_x$ ,  $V_y$  and  $V_z$  in Figure 13d, 13e and 13f.
- 574        (c) When the  $n_{CIS}$  disagrees in Figure 18g, 18h, 18i the distributions of  
 575        the OMNI  $V_x$ ,  $V_y$  and  $V_z$  are similar to the distributions of the OMNI  
 576         $V_x$ ,  $V_y$  and  $V_z$  in Figure 13d, 13e and 13f.
- 577        (d) When the  $n_{EFW}$  disagrees in simulations and measurements in Fig-  
 578        ure 18j, 18k, 18l the distributions of the OMNI  $V_x$ ,  $V_y$  and  $V_z$  are sim-  
 579        ilar to the distributions of the OMNI  $V_x$ ,  $V_y$  and  $V_z$  in Figure 13d, 13e  
 580        and 13f.

581        The distributions agree quite well because in Table 5 the number of the  
 582        poorly correlated intervals 18, 50, 33 and 30 for the  $B_z$ , the  $V_x$ , the  $n_{CIS}$   
 583        and  $n_{CIS}$  components, respectively. The number of cases are higher and  
 584        the values of the OMNI  $V_x$ ,  $V_y$  and  $V_z$  are not peculiar in the magne-  
 585        tosheath.

586        6. In the magnetosheath the distributions of the OMNI  $P$  can be compared  
 587        in Figure 13g and Figure 19a, 19b, 19c, 19d.

- 588        (a) When the  $B_z$  disagrees in Figure 19a the distribution of the OMNI  
 589         $P$  is similar to the distribution of the OMNI  $P$  in Figure 13g.
- 590        (b) When the  $V_x$  disagrees in simulations and measurements in Figure 19b  
 591        the distribution of the OMNI  $P$  is similar to the distributions of the  
 592        OMNI  $P$  in Figure 13g.
- 593        (c) When the  $n_{CIS}$  disagrees in simulations and measurements in Figure 19c  
 594        the distribution of the OMNI  $P$  is similar to the distributions of the  
 595        OMNI  $P$  in Figure 13g.
- 596        (d) When the  $n_{EFW}$  disagrees in simulations and measurements in Fig-  
 597        ure 19d the distribution of the OMNI  $P$  is similar to the distributions  
 598        of the OMNI  $P$  in Figure 13g.

599       **The distributions do not agree perfectly because in Table 5 the num-**  
 600       **ber of the poorly correlated intervals is only 6, 12 and 9 for the  $V_x$ , the**  
 601        **$n_{CIS}$  and  $n_{CIS}$  components, respectively. The distributions agree quite**  
 602       **well because in Table 5 the number of the poorly correlated intervals**  
 603       **18, 50, 33 and 30 for the  $B_z$ , the  $V_x$ , the  $n_{CIS}$  and  $n_{CIS}$  components, re-**  
 604       **spectively. The number of cases are higher and the values of the OMNI**  
 605        **$P$  are not peculiar in the magnetosheath.**

606       **The inaccuracy of the GUMICS-4 simulations does not depend on the OMNI**  
 607       **parameters in the solar wind and magnetosheath regions. The same study**  
 608       **does not need to be done for the magnetosphere because the deviance of the**  
 609       **measurements and the simulations is so large that it cannot be caused by the**  
 610       **wrong OMNI solar wind parameters.**

611       The bow shock positions agree in the GUMICS simulations and the Cluster SC3  
 612       measurements. However, the magnetopause locations do not fit well as the bow shock  
 613       in simulations and observations. In simulations the location of the magnetopause is de-  
 614       termined **from peaks in** currents density, particle density gradient, **or changes in flow**  
 615       **velocity** [Siscoe *et al.*, 2001; García and Hughes, 2007; Gordeev *et al.*, 2013, see refer-  
 616       ences therein]. In this paper the previously saved simulation parameters along the vir-  
 617       tual Cluster SC3 orbit are analysed. Therefore, the above mentioned methods cannot  
 618       be applied. The reason of the inaccuracy of the magnetopause positions in the simula-  
 619       tions must be the missing inner magnetosphere [...] module. This discrepancy of the  
 620       magnetopause location agrees with the results of Gordeev *et al.* [2013] and Facskó *et al.*  
 621       [2016]. Gordeev *et al.* [2013] compared synthetic GUMICS runs with **an** empirical for-  
 622       **formula for** the magnetopause locations. Facskó *et al.* [2016] used OMNI solar wind data  
 623       as input and got the same result as Gordeev *et al.* [2013] and this paper. Surprisingly  
 624       the neutral sheets are visible in both simulations and observations (Figure 20, Table 8).  
 625       This experience is exceptional because the night side magnetosphere of the GUMICS-4  
 626       simulations is small and twisted [Gordeev *et al.*, 2013; Facskó *et al.*, 2016]. However, in  
 627       these cases the IMF has no large  $B_y$  component. From Facskó *et al.* [2016] we know that  
 628       the GUMICS has normal long tail (or night side magnetosphere) if the  $B_y$  is small.

629    **5 Summary and conclusions**

630    Based on the previously created 1-year long GUMICS–4 run global MHD simu-  
 631    lation results are compared with Cluster SC3 magnetic field, solar wind velocity and den-  
 632    sity measurements along the spacecraft orbit. Intervals are selected when the Cluster SC3  
 633    and the virtual space probe are situated in the solar wind, magnetosheath and the mag-  
 634    netosphere and their correlation are calculated. Bow shock, magnetopause and neutral  
 635    sheet crossings are selected and their visibility and relative position are compared. We  
 636    achieved the following results:

- 637    1. In the solar wind the agreement of the  $B_z$ , the  $V_x$  and the  $n_{EFW}$  is very good, fur-  
     638    thermore the agreement of the  $n_{CIS}$  is also good.
- 639    2. In the magnetosheath the agreement of the magnetic field component, the ion plasma  
     640    moments and the calculated empirical density is a bit worse than in the solar wind.  
     641    The  $V_x$ , the  $n_{EFW}$  and the  $n_{CIS}$  fits better than the  $B_z$  component in the mag-  
     642    netosheath. Their agreement is still good. The reason of the deviation is the tur-  
     643    bulent behavior of the slowed down and thermalised turbulent solar wind.
- 644    3. In neither the dayside nor the nightside magnetosphere can the GUMICS–4 pro-  
     645    vide realistic results. The simulation outputs and the spacecraft measurement dis-  
     646    agree in this region. The reason of this deviation must be the missing coupled in-  
     647    inner magnetosphere model. The applied tilted dipole approach is not satisfactory  
     648    in the magnetosphere at all.
- 649    4. The GUMICS–4 code causes the deviations between the simulations and the space-  
     650    craft measurements because the upstream solar wind conditions seem to be nor-  
     651    mal when the disagreement of the different kinds of time series is large.
- 652    5. The position of the bow shock and the neutral sheet agrees well in the simulations  
     653    and the Cluster SC3 magnetic field, ion plasma moments and derived electron den-  
     654    sity measurements in this study. The position of the magnetopause does not fit  
     655    that well. The reason of this latest discrepancy must be the missing coupled in-  
     656    inner magnetosphere model too.

657    The GUMICS–4 has incredible scientific and strategic importance for the European Space  
 658    Weather and Scientific community. This code developed in the Finnish Meteorological  
 659    Institute is the most developed and tested, widely used tool for modelling the cosmic en-  
 660    viroment of the Earth in the old continent. [...] **An inner magnetosphere model should**

661 be two way coupled to the existing configuration of the simulation tool **to improve the**  
 662 **accuracy of the simulations.**

663 **Acknowledgments**

664 The OMNI data were obtained from the GSFC/SPDF OMNIWeb interface at <http://omniweb.gsfc.nasa.gov>.  
 665 The authors thank the FGM Team (PI: Chris Carr), the CIS Team (PI: Iannis Dandouras),  
 666 the WHISPER Team (PI: Jean-Louis Rauch), the EFW Team (PI: Mats Andre) and the  
 667 Cluster Science Archive for providing FGM magnetic field, CIS HIA ion plasma and WHIS-  
 668 PER electron density measurements. Data analysis was partly done with the QSAS sci-  
 669 ence analysis system provided by the United Kingdom Cluster Science Centre (Impe-  
 670 rial College London and Queen Mary, University of London) supported by the Science  
 671 and Technology Facilities Council (STFC). Eija Tanskanen acknowledges financial sup-  
 672 port from the Academy of Finland for the ReSoLVE Centre of Excellence (project No. 272157).  
 673 Gábor Facskó thanks Anna-Mária Vígh for improving the English of the paper. The au-  
 674 thors thank Pekka Janhunen for developing the GUMICS–4 code; furthermore Minna  
 675 Palmroth and Zoltán Vörös for the useful discussions. The work of Gábor Facskó was  
 676 supported by mission science funding for the Van Allen Probes mission, the American  
 677 Geophysical Union and the HAS Research Centre for Astronomy and Earth Sciences,  
 678 Sopron, Hungary. For further use of the year run data, [...] **request the authors or**  
 679 use the archive of the Community Coordinated Modelling Center (<https://ccmc.gsfc.nasa.gov/publications/posted>)

680

681 **References**

- 682 Balogh, A., M. W. Dunlop, S. W. H. Cowley, D. J. Southwood, J. G. Thomlinson,  
 683 K. H. Glassmeier, G. Musmann, H. Luhr, S. Buchert, M. H. Acuna, D. H. Fair-  
 684 field, J. A. Slavin, W. Riedler, K. Schwengenschuh, and M. G. Kivelson (1997),  
 685 The Cluster Magnetic Field Investigation, *Space Science Reviews*, 79, 65–91, doi:  
 686 10.1023/A:1004970907748.
- 687 Balogh, A., C. M. Carr, M. H. Acuña, M. W. Dunlop, T. J. Beek, P. Brown,  
 688 K. Fornaçon, E. Georgescu, K. Glassmeier, J. Harris, G. Musmann, T. Oddy, and  
 689 K. Schwengenschuh (2001), The Cluster Magnetic Field Investigation: overview of  
 690 in-flight performance and initial results, *Annales Geophysicae*, 19, 1207–1217.
- 691 Bartels, J., N. H. Heck, and H. F. Johnston (1939), The three-hour-range index mea-

- 692 suring geomagnetic activity, *Terrestrial Magnetism and Atmospheric Electricity*  
693 (*Journal of Geophysical Research*), 44, 411, doi:10.1029/TE044i004p00411.
- 694 Blagau, A., I. Dandouras, A. Barthe, S. Brunato, G. Facskó, and V. Constanti-  
695 nescu (2013), In-flight calibration of Hot Ion Analyser onboard Cluster, *Geo-  
696 scientific Instrumentation, Methods and Data Systems Discussions*, 3, 407–435,  
697 doi:10.5194/gid-3-407-2013.
- 698 Blagau, A., I. Dandouras, A. Barthe, S. Brunato, G. Facskó, and V. Constantinescu  
699 (2014), In-flight calibration of the Hot Ion Analyser on board Cluster, *Geoscientific  
700 Instrumentation, Methods and Data Systems*, 3, 49–58, doi:10.5194/gi-3-49-  
701 2014.
- 702 Chittenden, J. P., S. V. Lebedev, C. A. Jennings, S. N. Bland , and A. Ciardi  
703 (2004), X-ray generation mechanisms in three-dimensional simulations of wire  
704 array Z-pinches, *Plasma Physics and Controlled Fusion*, 46(12B), B457–B476,  
705 doi:10.1088/0741-3335/46/12B/039.
- 706 Ciardi, A., S. V. Lebedev, A. Frank, E. G. Blackman, J. P. Chittenden, C. J. Jen-  
707 nings, D. J. Ampleford, S. N. Bland, S. C. Bott, J. Rapley, G. N. Hall, F. A.  
708 Suzuki-Vidal, A. Marocchino, T. Lery, and C. Stehle (2007), The evolution of  
709 magnetic tower jets in the laboratory, *Physics of Plasmas*, 14(5), 056,501–056,501,  
710 doi:10.1063/1.2436479.
- 711 Credland, J., G. Mecke, and J. Ellwood (1997), The Cluster Mission: ESA'S  
712 Spacefleet to the Magnetosphere, *Space Science Reviews*, 79, 33–64, doi:  
713 10.1023/A:1004914822769.
- 714 Davis, T. N., and M. Sugiura (1966), Auroral electrojet activity index AE and its  
715 universal time variations, *Journal of Geophysical Research*, 71, 785–801, doi:  
716 10.1029/JZ071i003p00785.
- 717 Décréau, P. M. E., P. Fergeau, V. Krasnoselskikh, E. Le Guirriec, M. Lévéque,  
718 P. Martin, O. Randriamboarison, J. L. Rauch, F. X. Sené, H. C. Séran, J. G.  
719 Trotignon, P. Canu, N. Cornilleau, H. de Féraudy, H. Alleyne, K. Yearby, P. B.  
720 Mögensen, G. Gustafsson, M. André, D. C. Gurnett, F. Darrouzet, J. Lemaire,  
721 C. C. Harvey, P. Travnicek, and Whisper Experimenters Group (2001), Early re-  
722 sults from the Whisper instrument on Cluster: an overview, *Annales Geophysicae*,  
723 19, 1241–1258, doi:10.5194/angeo-19-1241-2001.
- 724 Escoubet, C. P., M. Fehringer, and M. Goldstein (2001), Introduction The Cluster

- mission, *Annales Geophysicae*, 19, 1197–1200, doi:10.5194/angeo-19-1197-2001.
- Facskó, G., I. Honkonen, T. Živković, L. Palin, E. Kallio, K. Ågren, H. Opgenoorth, E. I. Tanskanen, and S. Milan (2016), One year in the Earth's magnetosphere: A global MHD simulation and spacecraft measurements, *Space Weather*, 14, 351–367, doi:10.1002/2015SW001355.
- Facskó, G., T. B. Balogh, E. I. Anekallu, C. R. and Tanskanen, P. Peitso, L. Degener, M. Kangwa, T. Laitinen, and S. Laakso, H. Burley (in preparation), Bow shock identification in cluster measurements, *Space Weather*.
- Fazakerley, A. N., A. D. Lahiff, R. J. Wilson, I. Rozum, C. Anekallu, M. West, and H. Bacai (2010a), PEACE Data in the Cluster Active Archive, *Astrophysics and Space Science Proceedings*, 11, 129–144, doi:10.1007/978-90-481-3499-1\_8.
- Fazakerley, A. N., A. D. Lahiff, I. Rozum, D. Kataria, H. Bacai, C. Anekallu, M. West, and A. Åsnes (2010b), Cluster-PEACE In-flight Calibration Status, *Astrophysics and Space Science Proceedings*, 11, 281–299, doi:10.1007/978-90-481-3499-1\_19.
- García, K. S., and W. J. Hughes (2007), Finding the Lyon-Fedder-Mobarry magnetopause: A statistical perspective, *Journal of Geophysical Research (Space Physics)*, 112(A6), A06229, doi:10.1029/2006JA012039.
- Gordeev, E., G. Facskó, V. Sergeev, I. Honkonen, M. Palmroth, P. Janhunen, and S. Milan (2013), Verification of the GUMICS-4 global MHD code using empirical relationships, *Journal of Geophysical Research (Space Physics)*, 118, 3138–3146, doi:10.1002/jgra.50359.
- Greenwald, R. A., K. B. Baker, J. R. Dudeney, M. Pinnock, T. B. Jones, E. C. Thomas, J.-P. Villain, J.-C. Cerisier, C. Senior, C. Hanuise, R. D. Hunsucker, G. Sofko, J. Koehler, E. Nielsen, R. Pellinen, A. D. M. Walker, N. Sato, and H. Yamagishi (1995), Darn/Superdarn: A Global View of the Dynamics of High-Latitude Convection, *Space Science Reviews*, 71, 761–796, doi:10.1007/BF00751350.
- Guild, T. B., H. E. Spence, E. L. Kepko, V. Merkin, J. G. Lyon, M. Wiltberger, and C. C. Goodrich (2008a), Geotail and LFM comparisons of plasma sheet climatology: 1. Average values, *Journal of Geophysical Research (Space Physics)*, 113, A04216, doi:10.1029/2007JA012611.
- Guild, T. B., H. E. Spence, E. L. Kepko, V. Merkin, J. G. Lyon, M. Wiltberger, and

- 758 C. C. Goodrich (2008b), Geotail and LFM comparisons of plasma sheet climatol-  
759 ogy: 2. Flow variability, *Journal of Geophysical Research (Space Physics)*, 113,  
760 A04217, doi:10.1029/2007JA012613.
- 761 Gustafsson, G., R. Bostrom, B. Holback, G. Holmgren, A. Lundgren, K. Stasiewicz,  
762 L. Ahlen, F. S. Mozer, D. Pankow, P. Harvey, P. Berg, R. Ulrich, A. Pedersen,  
763 R. Schmidt, A. Butler, A. W. C. Fransen, D. Klinge, M. Thomsen, C.-G. Faltham-  
764 mar, P.-A. Lindqvist, S. Christenson, J. Holtet, B. Lybekk, T. A. Sten, P. Tan-  
765 skanen, K. Lappalainen, and J. Wygant (1997), The Electric Field and Wave  
766 Experiment for the Cluster Mission, *Space Science Reviews*, 79, 137–156, doi:  
767 10.1023/A:1004975108657.
- 768 Gustafsson, G., M. André, T. Carozzi, A. I. Eriksson, C.-G. Fälthammar, R. Grard,  
769 G. Holmgren, J. A. Holtet, N. Ivchenko, T. Karlsson, Y. Khotyaintsev, S. Klimov,  
770 H. Laakso, P.-A. Lindqvist, B. Lybekk, G. Marklund, F. Mozer, K. Mursula,  
771 A. Pedersen, B. Popielawska, S. Savin, K. Stasiewicz, P. Tanskanen, A. Vaivads,  
772 and J.-E. Wahlund (2001), First results of electric field and density observations  
773 by Cluster EFW based on initial months of operation, *Annales Geophysicae*, 19,  
774 1219–1240, doi:10.5194/angeo-19-1219-2001.
- 775 Haiducek, J. D., D. T. Welling, N. Y. Ganushkina, S. K. Morley, and D. S. Oz-  
776 turk (2017), SWMF Global Magnetosphere Simulations of January 2005: Geo-  
777 magnetic Indices and Cross-Polar Cap Potential, *Space Weather*, 15, 1567–1587,  
778 doi:10.1002/2017SW001695.
- 779 Iyemori, T. (1990), Storm-time magnetospheric currents inferred from mid-latitude  
780 geomagnetic field variations, *Journal of Geomagnetism and Geoelectricity*, 42,  
781 1249–1265, doi:10.5636/jgg.42.1249.
- 782 Janhunen, P., M. Palmroth, T. Laitinen, I. Honkonen, L. Juusola, G. Facskó, and  
783 T. I. Pulkkinen (2012), The GUMICS-4 global MHD magnetosphere-ionosphere  
784 coupling simulation, *Journal of Atmospheric and Solar-Terrestrial Physics*, 80,  
785 48–59, doi:10.1016/j.jastp.2012.03.006.
- 786 Johnstone, A. D., C. Alsop, S. Burge, P. J. Carter, A. J. Coates, A. J. Coker, A. N.  
787 Fazakerley, M. Grande, R. A. Gowen, C. Gurgiolo, B. K. Hancock, B. Narheim,  
788 A. Preece, P. H. Sheather, J. D. Winningham, and R. D. Woodliffe (1997), Peace:  
789 a Plasma Electron and Current Experiment, *Space Science Reviews*, 79, 351–398,  
790 doi:10.1023/A:1004938001388.

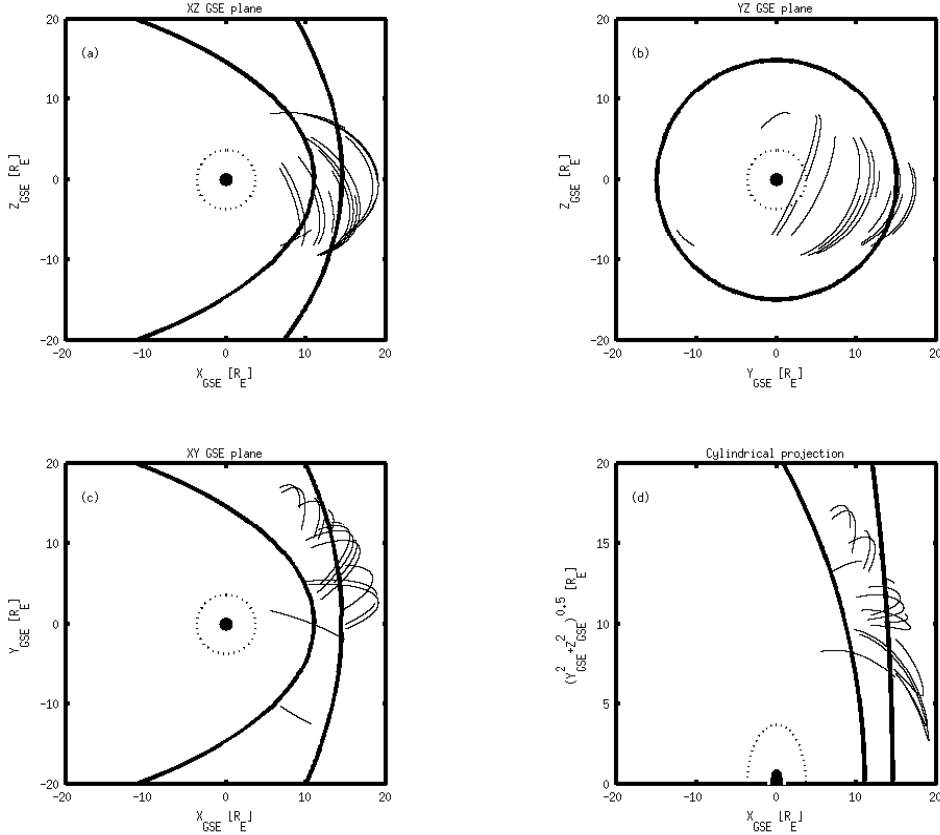
- 791 Juusola, L., O. Amm, K. Kauristie, and A. Viljanen (2007), A model for estimating  
792 the relation between the Hall to Pedersen conductance ratio and ground magnetic  
793 data derived from CHAMP satellite statistics, *Annales Geophysicae*, *25*, 721–736,  
794 doi:10.5194/angeo-25-721-2007.
- 795 Juusola, L., G. Facskó, I. Honkonen, P. Janhunen, H. Vanhamäki, K. Kauristie,  
796 T. V. Laitinen, S. E. Milan, M. Palmroth, E. I. Tanskanen, and A. Viljanen  
797 (2014), Statistical comparison of seasonal variations in the GUMICS-4 global  
798 MHD model ionosphere and measurements, *Space Weather*, *12*, 582–600, doi:  
799 10.1002/2014SW001082.
- 800 Kallio, E., and G. Facskó (2015), Properties of plasma near the moon in the magne-  
801 totail, *Planetary and Space Science*, *115*, 69–76, doi:10.1016/j.pss.2014.11.007.
- 802 Kokubun, S., T. Yamamoto, M. H. Acuña, K. Hayashi, K. Shiokawa, and H. Kawano  
803 (1994), The GEOTAIL Magnetic Field Experiment., *Journal of Geomagnetism*  
804 and *Geoelectricity*, *46*, 7–21, doi:10.5636/jgg.46.7.
- 805 Lakka, A., T. I. Pulkkinen, A. P. Dimmock, M. Myllys, I. Honkonen, and M. Palm-  
806 roth (2018a), The Cross-Polar Cap Saturation in GUMICS-4 During High Solar  
807 Wind Driving, *Journal of Geophysical Research (Space Physics)*, *123*, 3320–3332,  
808 doi:10.1002/2017JA025054.
- 809 Lakka, A., T. I. Pulkkinen, A. P. Dimmock, E. Kilpua, M. Ala-Lahti, I. Honko-  
810 nen, M. Palmroth, and Raukunen (2018b), Icme impact at earth with low and  
811 typical mach number plasma characteristics, *Annales Geophysicae Discussions*,  
812 <https://doi.org/10.5194/angeo-2018-81>.
- 813 Lani, A., A. Sanna, N. Villedieu, and M. Panesi (2012), COOLFluiD an Open Com-  
814 putational Platform for Aerothermodynamics and Flow-Radiation Coupling, in  
815 *ESA Special Publication, ESA Special Publication*, vol. 714, p. 45.
- 816 Lyon, J. G., J. A. Fedder, and C. M. Mobarry (2004), The Lyon-Fedder-Mobarry  
817 (LFM) global MHD magnetospheric simulation code, *Journal of Atmospheric and*  
818 *Solar-Terrestrial Physics*, *66*, 1333–1350, doi:10.1016/j.jastp.2004.03.020.
- 819 Mejnertsen, L., J. P. Eastwood, J. P. Chittenden, and A. Masters (2016), Global  
820 MHD simulations of Neptune’s magnetosphere, *Journal of Geophysical Research*  
821 (*Space Physics*), *121*(8), 7497–7513, doi:10.1002/2015JA022272.
- 822 Mejnertsen, L., J. P. Eastwood, H. Hietala, S. J. Schwartz, and J. P. Chittenden  
823 (2018), Global MHD Simulations of the Earth’s Bow Shock Shape and Motion

- 824 Under Variable Solar Wind Conditions, *Journal of Geophysical Research (Space*  
825 *Physics)*, 123(1), 259–271, doi:10.1002/2017JA024690.
- 826 Mukai, T., S. Machida, Y. Saito, M. Hirahara, T. Terasawa, N. Kaya, T. Obara,  
827 M. Ejiri, and A. Nishida (1994), The Low Energy Particle (LEP) Experiment on-  
828 board the GEOTAIL Satellite., *Journal of Geomagnetism and Geoelectricity*, 46,  
829 669–692, doi:10.5636/jgg.46.669.
- 830 Peredo, M., J. A. Slavin, E. Mazur, and S. A. Curtis (1995), Three-dimensional po-  
831 sition and shape of the bow shock and their variation with Alfvénic, sonic and  
832 magnetosonic Mach numbers and interplanetary magnetic field orientation, *Jour-*  
833 *nal of Geophysical Research*, 100, 7907–7916, doi:10.1029/94JA02545.
- 834 Poedts, S., A. Kochanov, A. Lani, C. Scolini, C. Verbeke, S. Hosteaux, E. Chané,  
835 H. Deconinck, N. Mihalache, F. Diet, D. Heynderickx, J. De Keyser, E. De  
836 Donder, N. B. Crosby, M. Echim, L. Rodriguez, R. Vansintjan, F. Verstringe,  
837 B. Mampaey, R. Horne, S. Glauert, P. Jiggens, R. Keil, A. Glover, G. Deprez, and  
838 J.-P. Luntama (2020), The Virtual Space Weather Modelling Centre, *Journal of*  
839 *Space Weather and Space Climate*, 10, 14, doi:10.1051/swsc/2020012.
- 840 Powell, K. G., P. L. Roe, T. J. Linde, T. I. Gombosi, and D. L. De Zeeuw (1999), A  
841 Solution-Adaptive Upwind Scheme for Ideal Magnetohydrodynamics, *Journal of*  
842 *Computational Physics*, 154, 284–309, doi:10.1006/jcph.1999.6299.
- 843 Raeder, J., D. Larson, W. Li, E. L. Kepko, and T. Fuller-Rowell (2008), OpenG-  
844 GCM Simulations for the THEMIS Mission, *Space Science Reviews*, 141, 535–555,  
845 doi:10.1007/s11214-008-9421-5.
- 846 Reigber, C., H. Lühr, and P. Schwintzer (2002), CHAMP mission status, *Advances*  
847 *in Space Research*, 30, 129–134, doi:10.1016/S0273-1177(02)00276-4.
- 848 Reme, H., J. M. Bosqued, J. A. Sauvaud, A. Cros, J. Dandouras, C. Aoustin,  
849 J. Bouyssou, T. Camus, J. Cuvilo, C. Martz, J. L. Medale, H. Perrier, D. Rome-  
850 fort, J. Rouzaud, C. D'Uston, E. Mobius, K. Crocker, M. Granoff, L. M. Kistler,  
851 M. Popecki, D. Hovestadt, B. Klecker, G. Paschmann, M. Scholer, C. W. Carl-  
852 son, D. W. Curtis, R. P. Lin, J. P. McFadden, V. Formisano, E. Amata, M. B.  
853 Bavassano-Cattaneo, P. Baldetti, G. Bellucci, R. Bruno, G. Chionchio, A. di Lel-  
854 lis, E. G. Shelley, A. G. Ghielmetti, W. Lennartsson, A. Korth, H. Rosenbauer,  
855 R. Lundin, S. Olsen, G. K. Parks, M. McCarthy, and H. Balsiger (1997), The  
856 Cluster Ion Spectrometry (CIS) Experiment, *Space Science Reviews*, 79, 303–350,

- 857 doi:10.1023/A:1004929816409.
- 858 Rème, H., C. Aoustin, J. M. Bosqued, I. Dandouras, B. Lavraud, J. A. Sauvaud,  
859 A. Barthe, J. Bouyssou, T. Camus, O. Coeur-Joly, A. Cros, J. Cuvilo, F. Ducay,  
860 Y. Garbarowitz, J. L. Medale, E. Penou, H. Perrier, D. Romefort, J. Rouzaud,  
861 C. Vallat, D. Alcaydé, C. Jacquay, C. Mazelle, C. D'Uston, E. Möbius, L. M.  
862 Kistler, K. Crocker, M. Granoff, C. Mouikis, M. Popecki, M. Vosbury, B. Klecker,  
863 D. Hovestadt, H. Kucharek, E. Kuenneth, G. Paschmann, M. Scholer, N. Sckopke,  
864 E. Seidenschwang, C. W. Carlson, D. W. Curtis, C. Ingraham, R. P. Lin, J. P.  
865 McFadden, G. K. Parks, T. Phan, V. Formisano, E. Amata, M. B. Bavassano-  
866 Cattaneo, P. Baldetti, R. Bruno, G. Chionchio, A. di Lellis, M. F. Marcucci,  
867 G. Pallocchia, A. Korth, P. W. Daly, B. Graeve, H. Rosenbauer, V. Vasyliunas,  
868 M. McCarthy, M. Wilber, L. Eliasson, R. Lundin, S. Olsen, E. G. Shelley, S. Fuseli-  
869 er, A. G. Ghielmetti, W. Lennartsson, C. P. Escoubet, H. Balsiger, R. Friedel, J.-  
870 B. Cao, R. A. Kovrashkin, I. Papamastorakis, R. Pellat, J. Scudder, and B. Son-  
871 nerup (2001), First multispacecraft ion measurements in and near the Earth's  
872 magnetosphere with the identical Cluster ion spectrometry (CIS) experiment,  
873 *Annales Geophysicae*, 19, 1303–1354, doi:10.5194/angeo-19-1303-2001.
- 874 Ritter, P., H. Lühr, A. Viljanen, O. Amm, A. Pulkkinen, and I. Sillanpää (2004),  
875 Ionospheric currents estimated simultaneously from CHAMP satellite and IMAGE  
876 ground-based magnetic field measurements: a statistical study at auroral latitudes,  
877 *Annales Geophysicae*, 22, 417–430, doi:10.5194/angeo-22-417-2004.
- 878 Rostoker, G. (1972), Geomagnetic indices., *Reviews of Geophysics and Space  
879 Physics*, 10, 935–950, doi:10.1029/RG010i004p00935.
- 880 Siscoe, G. L., G. M. Erickson, B. U. Sonnerup, N. C. Maynard, J. A. Schoendorf,  
881 K. D. Siebert, D. R. Weimer, W. W. White, and G. R. Wilson (2001), The Mag-  
882 netospheric Fluopause, in *AGU Spring Meeting Abstracts*, vol. 2001, pp. SM52D–  
883 02.
- 884 Sofko, G. J., R. Greenwald, and W. Bristow (1995), Direct determination of large-  
885 scale magnetospheric field-aligned currents with SuperDARN, *Geophysical Re-  
886 search Letters*, 22, 2041–2044, doi:10.1029/95GL01317.
- 887 Thomsen, M. F. (2004), Why  $K_p$  is such a good measure of magnetospheric convec-  
888 tion, *Space Weather*, 2, S11004, doi:10.1029/2004SW000089.
- 889 Tóth, G., I. V. Sokolov, T. I. Gombosi, D. R. Chesney, C. R. Clauer, D. L. de

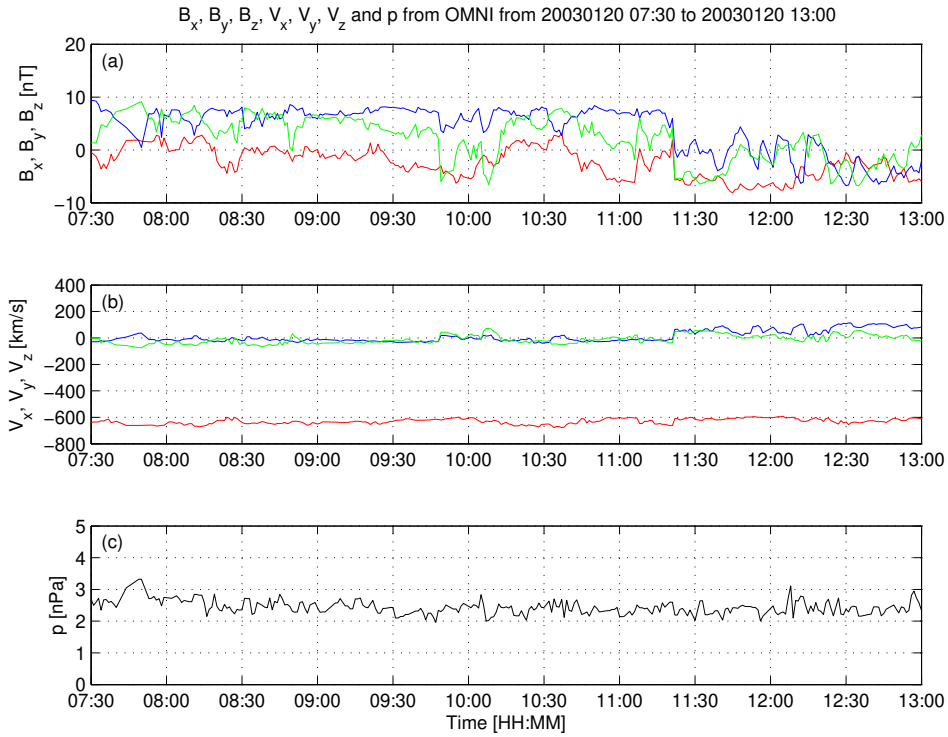
- 890 Zeeuw, K. C. Hansen, K. J. Kane, W. B. Manchester, R. C. Oehmke, K. G. Pow-  
891 ell, A. J. Ridley, I. I. Roussev, Q. F. Stout, O. Volberg, R. A. Wolf, S. Sazykin,  
892 A. Chan, B. Yu, and J. Kóta (2005), Space Weather Modeling Framework: A  
893 new tool for the space science community, *Journal of Geophysical Research (Space*  
894 *Physics)*, 110, A12226, doi:10.1029/2005JA011126.
- 895 Tóth, G., B. van der Holst, I. V. Sokolov, D. L. De Zeeuw, T. I. Gombosi, F. Fang,  
896 W. B. Manchester, X. Meng, D. Najib, K. G. Powell, Q. F. Stout, A. Glo-  
897 cer, Y.-J. Ma, and M. Opher (2012), Adaptive numerical algorithms in space  
898 weather modeling, *Journal of Computational Physics*, 231, 870–903, doi:  
899 10.1016/j.jcp.2011.02.006.
- 900 Trotignon, J. G., P. M. E. Décréau, J. L. Rauch, X. Vallières, A. Rochel,  
901 S. Kougblénou, G. Lointier, G. Facskó, P. Canu, F. Darrouzet, and A. Masson  
902 (2010), The WHISPER Relaxation Sounder and the CLUSTER Active Archive,  
903 *Astrophysics and Space Science Proceedings*, 11, 185–208, doi:10.1007/978-90-481-  
904 3499-1\_12.
- 905 Trotignon, J.-G., Vallières, and the WHISPER team (2011), Calibration report of  
906 the whisper measurements in the cluster active archive (caa), *Tech. rep.*, LPC2E  
907 CNRS, caa-est-cr-whi.
- 908 Tsyganenko, N. A. (1995), Modeling the Earth's magnetospheric magnetic field  
909 confined within a realistic magnetopause, *Journal of Geophysical Research*, 100,  
910 5599–5612, doi:10.1029/94JA03193.
- 911 Vörös, Z., G. Facskó, M. Khodachenko, I. Honkonen, P. Janhunen, and M. Palmroth  
912 (2014), Windsock memory COnditioned RAM (CO-RAM) pressure effect: Forced  
913 reconnection in the Earth's magnetotail, *Journal of Geophysical Research (Space*  
914 *Physics)*, 119, 6273–6293, doi:10.1002/2014JA019857.
- 915 Wang, Z.-D., and R. L. Xu (1994), Signatures of the magnetotail neutral sheet,  
916 *Geophysical Research Letters*, 21(19), 2087–2090, doi:10.1029/94GL01960.
- 917 Weimer, D. R. (2005), Improved ionospheric electrodynamic models and applica-  
918 tion to calculating Joule heating rates, *Journal of Geophysical Research (Space*  
919 *Physics)*, 110, A05306, doi:10.1029/2004JA010884.
- 920 Wiltberger, M., E. J. Rigler, V. Merkin, and J. G. Lyon (2017), Structure of High  
921 Latitude Currents in Magnetosphere-Ionosphere Models, *Space Science Reviews*,  
922 206, 575–598, doi:10.1007/s11214-016-0271-2.

- 923 Zhang, B., W. Lotko, M. J. Wiltberger, O. J. Brambles, and P. A. Damiano (2011),  
924 A statistical study of magnetosphere-ionosphere coupling in the Lyon-Fedder-  
925 Mobarry global MHD model, *Journal of Atmospheric and Solar-Terrestrial  
926 Physics*, 73, 686–702, doi:10.1016/j.jastp.2010.09.027.
- 927 Zhang, B., K. A. Sorathia, J. G. Lyon, V. G. Merkin, J. S. Garretson, and M. Wilt-  
928 berger (2019), GAMERA: A Three-dimensional Finite-volume MHD Solver for  
929 Non-orthogonal Curvilinear Geometries, *The Astrophysical Journal Supplement  
930 Series*, 244(1), 20, doi:10.3847/1538-4365/ab3a4c.

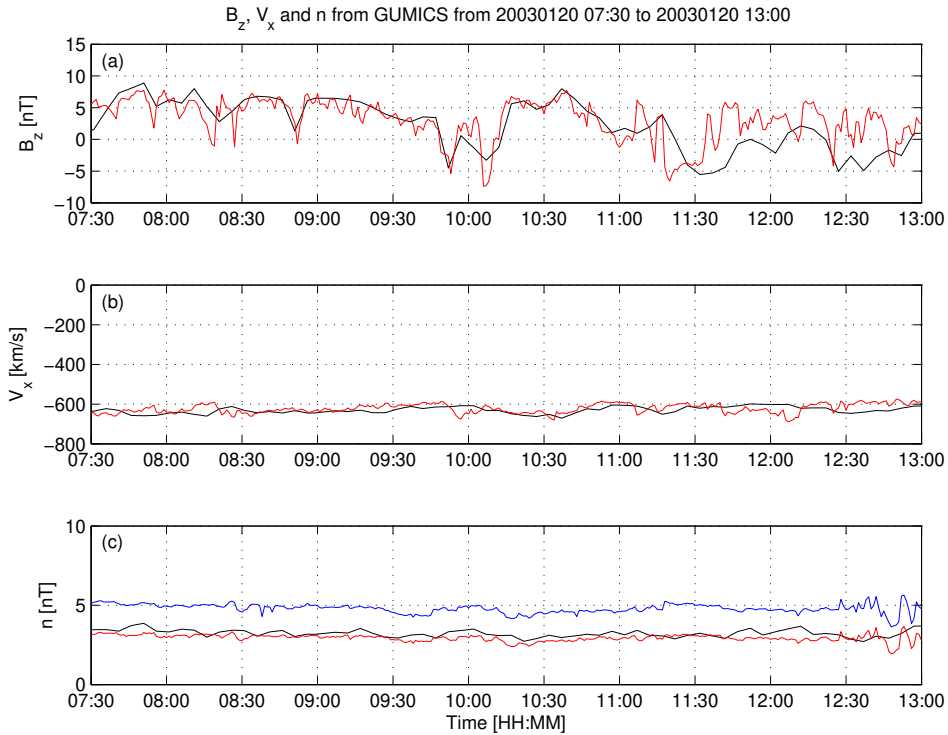


931 **Figure 1.** Cluster SC3 orbit in the solar wind in GSE system for all intervals (see Table 1).

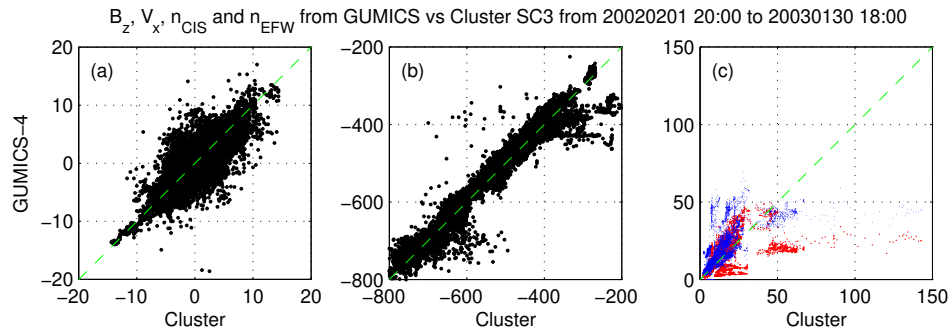
932 (a) XZ (b) YZ (c) XY (d) Cylindrical projection. Average bow-shock and magnetopause posi-  
 933 tions are drawn on all plots using [thick](#) solid lines [Perego *et al.*, 1995; Tsyganenko, 1995, respec-  
 934 tively]. The black dots at  $3.7 R_E$  show the boundary of the GUMICS-4 inner magnetospheric  
 935 domain. The black circle in the origo of all plots shows the size of the Earth.



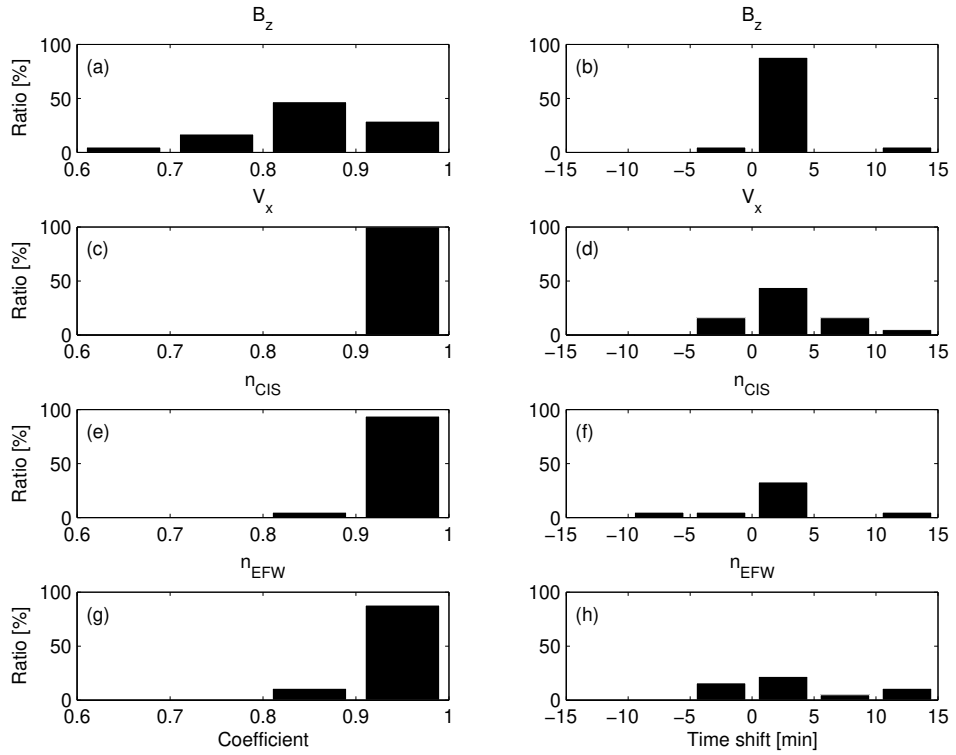
936 **Figure 2.** OMNI solar wind data in GSE system from 7:30 to 13:00 (UT) on January 20,  
937 2003. (a) Magnetic field  $B_x$  (red),  $B_y$  (green) and  $B_z$  (blue) components. (b) Solar wind velocity  
938  $V_x$  (red),  $V_y$  (green) and  $V_z$  (blue) components. (c) The  $P$  pressure of the solar wind (black).



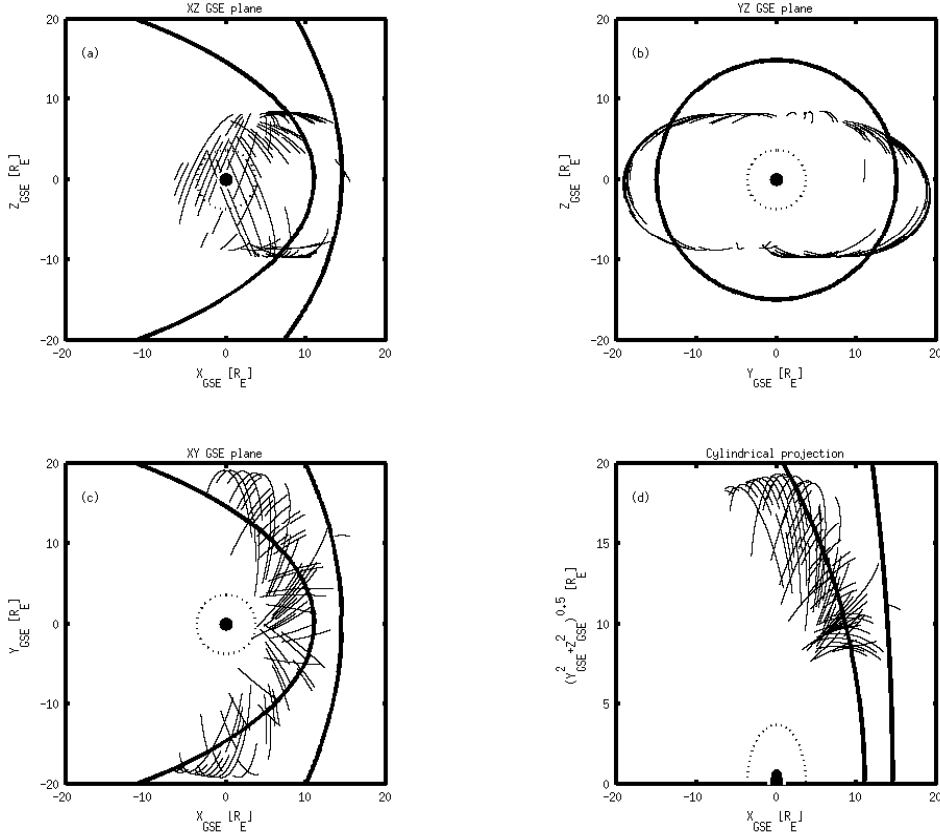
939 **Figure 3.** GUMICS-4 simulation results (black) and Cluster SC3 magnetic field Z component,  
 940 ion plasma moments (red) and electron density calculated from spacecraft potential (blue) from  
 941 January 20, 2003 from 7:30 to 13:00 (UT) in the solar wind in GSE system. (a) Magnetic field Z  
 942 component. (b) Solar wind velocity X component (c) Solar wind density.



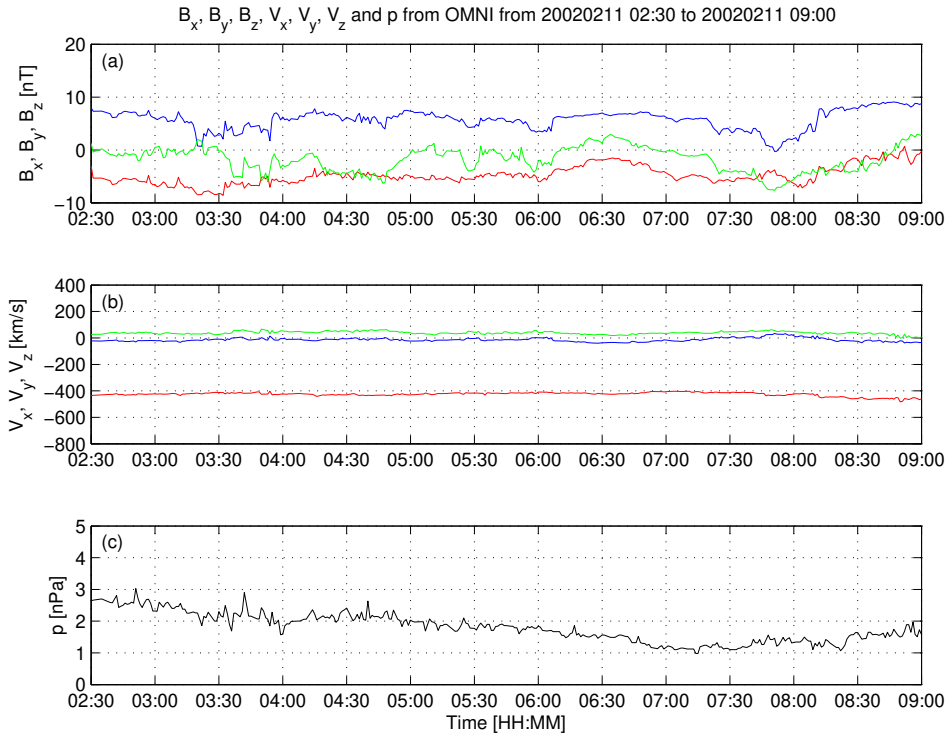
943 **Figure 4.** Scattered plots of the Cluster SC3 and GUMICS-4 simulations for all intervals in  
 944 the solar wind. The dashed line is the  $y=x$  line. (a) Magnetic field Z component in GSE system.  
 945 (b) Solar wind velocity X component in GSE system. (c) Solar wind density measured by the  
 946 CIS HIA instrument (red) and calculated from the spacecraft potential (blue).



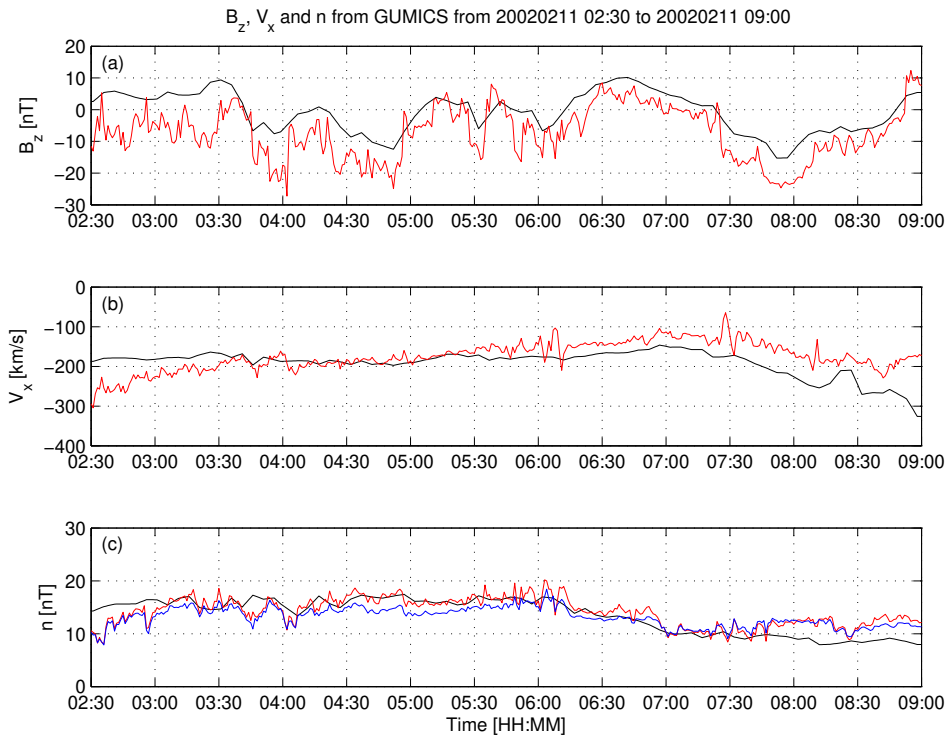
947 **Figure 5.** The distributions of the **highest** correlation coefficients (a, c, e, g) of the magnetic  
 948 field Z component ( $B_z$ ) in GSE system, solar wind velocity X component ( $V_x$ ) in GSE system,  
 949 the solar wind density measured by the CIS HIA ( $n_{CIS}$ ) instrument and calculated from the  
 950 spacecraft potential ( $n_{EFW}$ ), respectively, for all intervals in the solar wind. The distributions  
 951 of the **corresponding** time shifts (b, d, f, h) of the  $B_z$ , the  $V_x$ , the  $n_{CIS}$  and the  $n_{EFW}$ , respec-  
 952 tively, for all intervals in the solar wind.



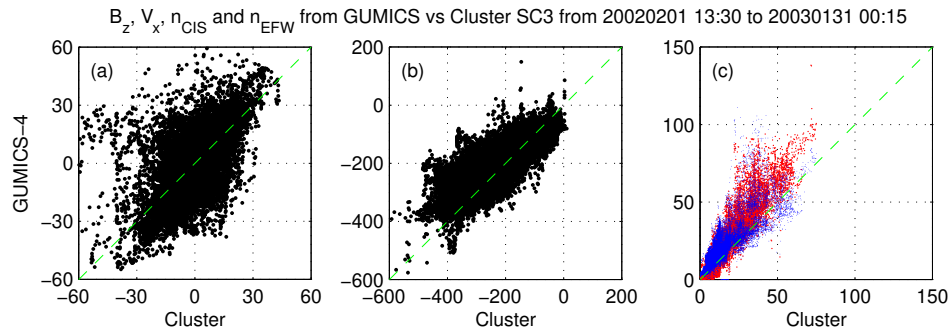
953 **Figure 6.** Cluster SC3 orbit in the magnetosheath in GSE system for all intervals (see Ta-  
954 ble 2). (a) XZ (b) YZ (c) XY (d) Cylindrical projection. Average bow-shock and magnetopause  
955 positions are drawn on all plots using [thick](#) solid lines [Peredo *et al.*, 1995; Tsyganenko, 1995,  
956 respectively]. The black dots at  $3.7 R_E$  show the boundary of the GUMICS-4 inner magneto-  
957 spheric domain. The black circle in the origo of all plots shows the size of the Earth.



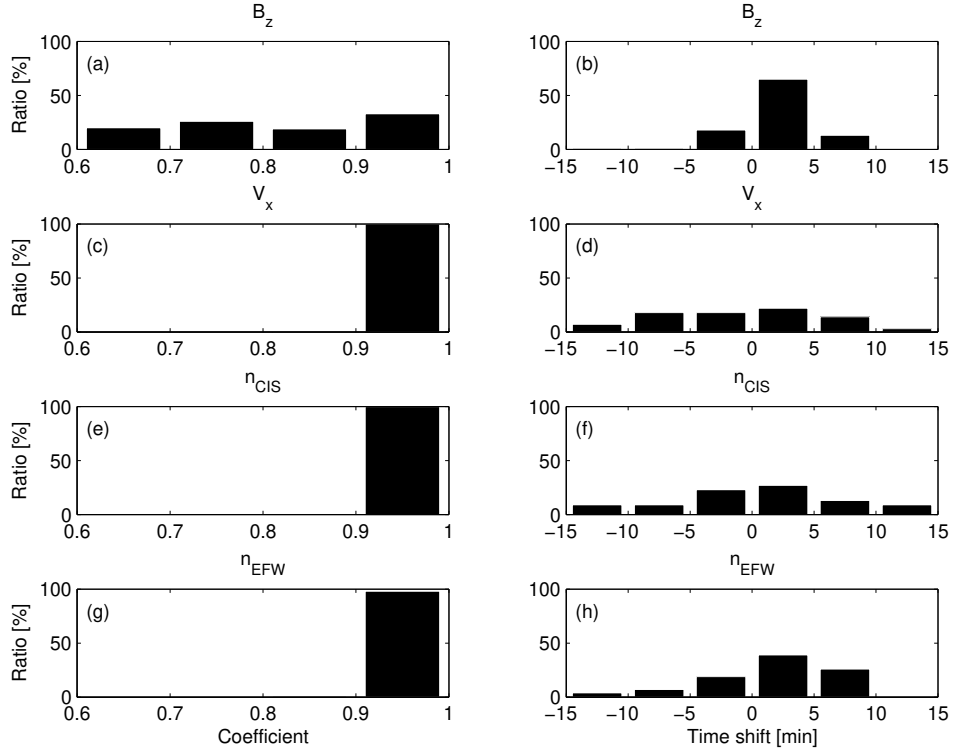
958 **Figure 7.** OMNI solar wind data in GSE system from 2:30 to 09:00 (UT) on February 11,  
959 2002. (a) Magnetic field  $B_x$  (red),  $B_y$  (green) and  $B_z$  (blue) components. (b) Solar wind velocity  
960  $V_x$  (red),  $V_y$  (green) and  $V_z$  (blue) components. (c) The  $P$  pressure of the solar wind (black).



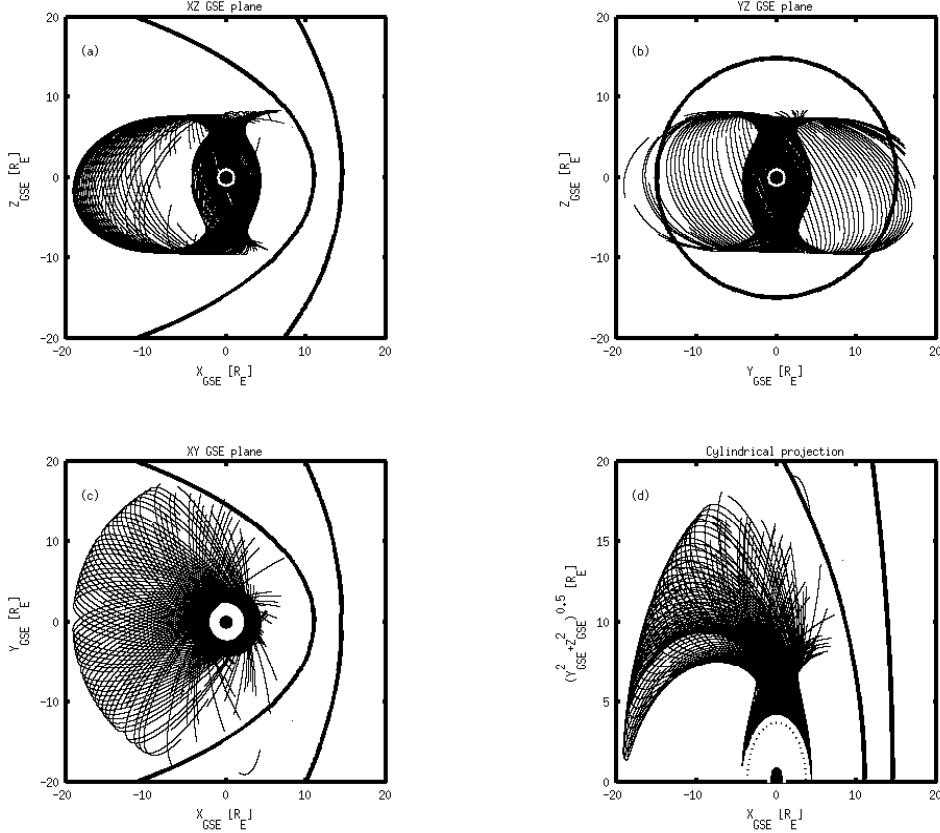
961      **Figure 8.** GUMICS-4 simulation results (black) and Cluster SC3 magnetic field Z component,  
 962      ion plasma moments (red) and electron density calculated from spacecraft potential (blue) from  
 963      February 11, 2002 from 2:30 to 9:00 (UT) in the magnetosheath in GSE system (a) Magnetic  
 964      field Z component. (b) Solar wind velocity X component (c) Solar wind density.



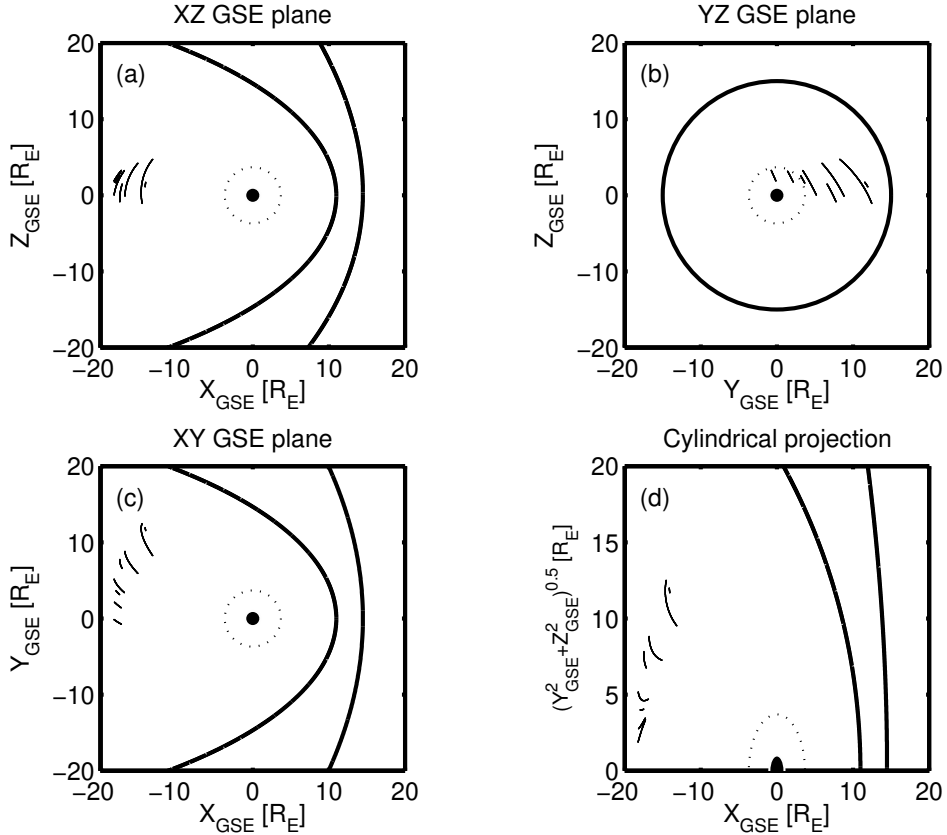
965 **Figure 9.** Scattered plots of the Cluster SC3 and GUMICS-4 simulations for all intervals in  
 966 the magnetosheath in GSE system. The dashed line is the  $y=x$  line. (a) Magnetic field Z com-  
 967 ponent. (b) Solar wind velocity X component. (c) Solar wind density measured by the CIS HIA  
 968 instrument (red) and calculated from the spacecraft potential (blue).



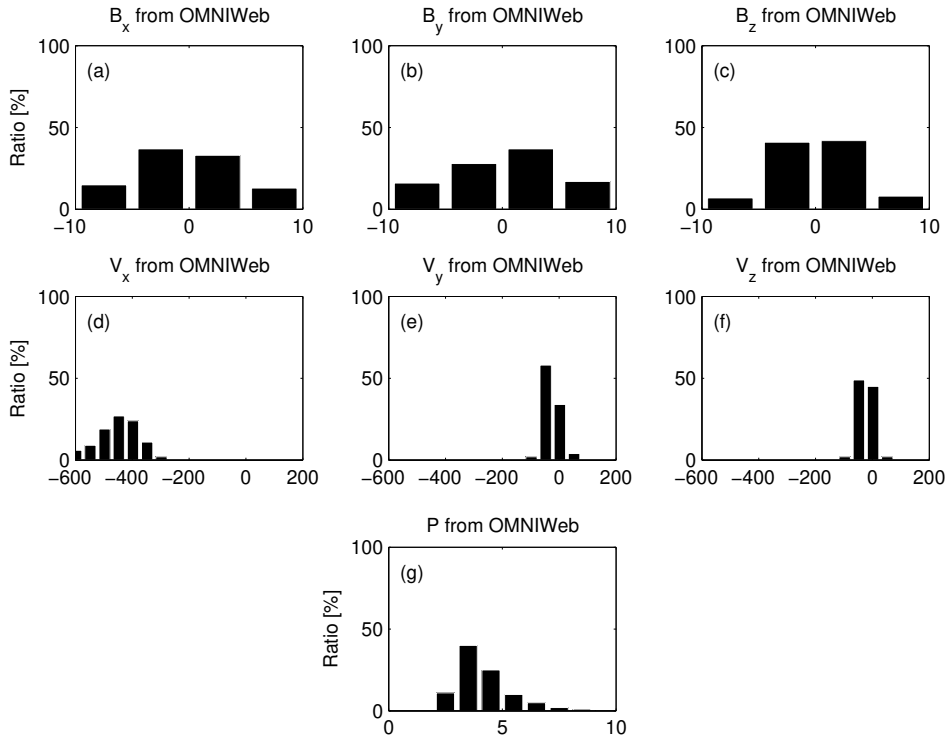
969      **Figure 10.** The distributions of the correlation coefficients (a, c, e, g) of the magnetic field Z  
 970      component ( $B_z$ ) in GSE system, solar wind velocity X component ( $V_x$ ) in GSE system, the solar  
 971      wind density measured by the CIS HIA ( $n_{CIS}$ ) instrument and calculated from the spacecraft  
 972      potential ( $n_{EFW}$ ), respectively, for all intervals in the magnetosheath. The distributions of the  
 973      time shifts (b, d, f, h) of the  $B_z$ , the  $V_x$ , the  $n_{CIS}$  and the  $n_{EFW}$ , respectively, for all intervals  
 974      in the magnetosheath.



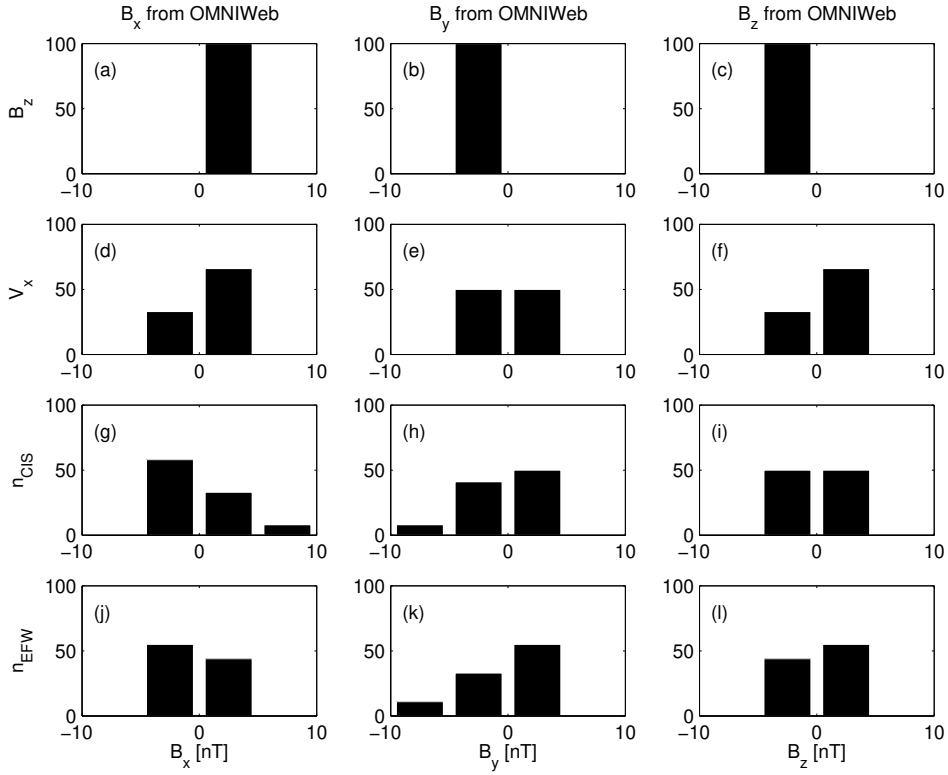
975 **Figure 11.** Cluster SC3 orbit in the magnetosphere in GSE system for all intervals (see Ta-  
 976 ble 3). (a) XZ (b) YZ (c) XY (d) Cylindrical projection. Average bow-shock and magnetopause  
 977 positions are drawn on all plots using **thick** solid lines [Peredo *et al.*, 1995; Tsyganenko, 1995,  
 978 respectively]. The black dots at  $3.7 R_E$  show the boundary of the GUMICS-4 inner magneto-  
 979 spheric domain. The black circle in the origo of all plots shows the size of the Earth.



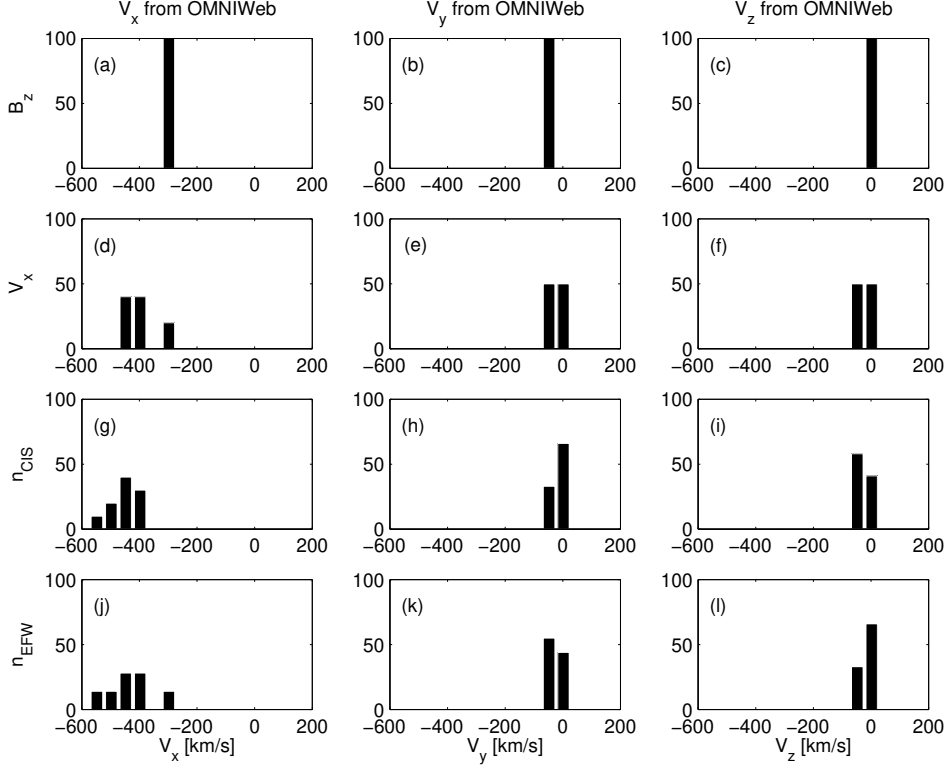
980 **Figure 12.** Cluster SC3 orbit in the tail in GSE system for all intervals (see Table 8). (a) XZ  
 981 (b) YZ (c) XY (d) Cylindrical projection. Average bow-shock and magnetopause positions are  
 982 drawn on all plots using thick solid lines [Perego *et al.*, 1995; Tsyganenko, 1995, respectively].  
 983 The black dots at  $3.7 R_E$  show the boundary of the GUMICS-4 inner magnetospheric domain.  
 984 The black circle in the origo of all plots shows the size of the Earth.



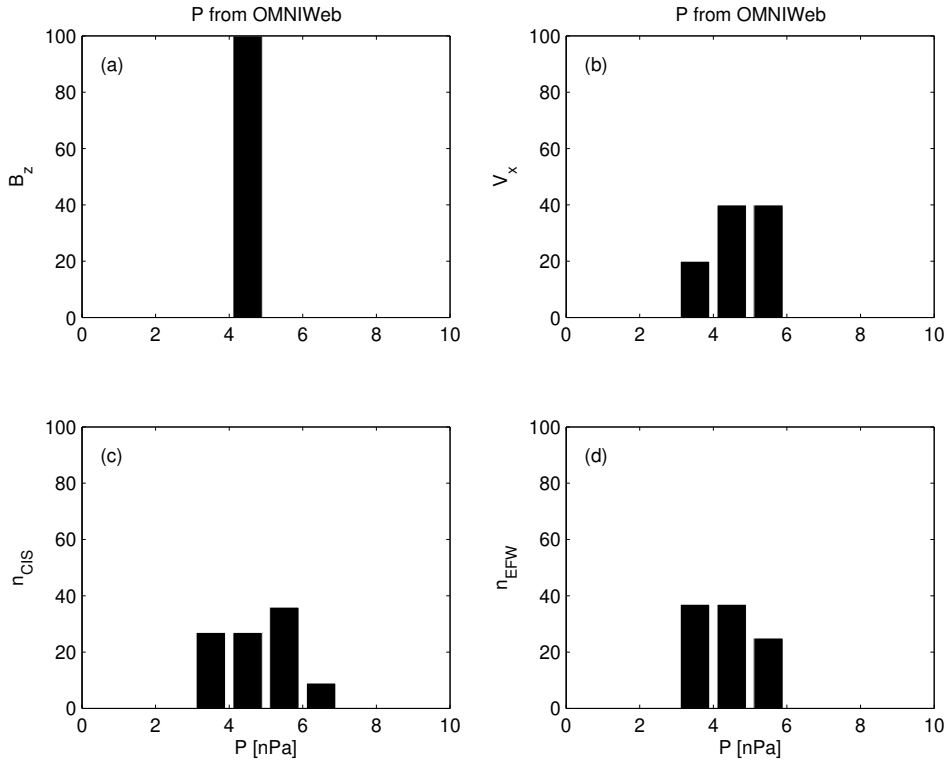
985      **Figure 13.** (a, b, c) The distributions of the OMNI solar wind magnetic field ( $B_x$ ,  $B_y$ ,  $B_z$ )  
 986      components, (d, e, f) the OMNI solar wind velocity ( $V_x$ ,  $V_y$ ,  $V_z$ ) components and (g) the solar  
 987      wind dynamic pressure during the 1-year run from January 29, 2002 to February 2, 2003 in GSE  
 988      reference frame, respectively. The relative values are given on the vertical axis of all plots in  
 989      percentage.



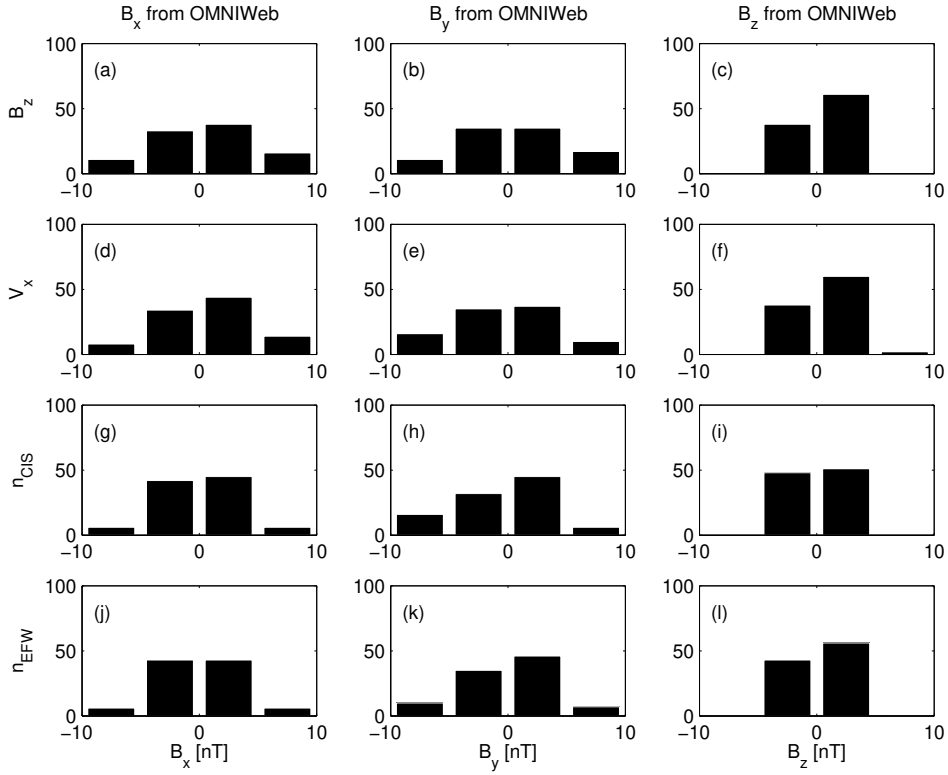
990 **Figure 14.** The distributions of the  $B_x$ , the  $B_y$  and the  $B_z$  OMNI solar wind magnetic field  
991 components when the agreement of the Cluster SC3 measurements and the GUMICS–4 simu-  
992 lations are poor in the solar wind (see Table 4). The  $B_z$ , the  $V_x$ , the  $n_{CIS}$  and the  $n_{EFW}$  are  
993 the magnetic field GSE Z component, the plasma ion velocity X GSE component, the solar wind  
994 density measured by the CIS HIA instrument and the calculated from the EFW spacecraft po-  
995 tential, respectively. (a, b, c) Distribution of OMNI  $B_x$ ,  $B_y$ ,  $B_z$  when the agreement of  $B_z$  is  
996 poor. (d, e, f) Distribution of OMNI  $B_x$ ,  $B_y$ ,  $B_z$  when the agreement of  $V_x$  is poor. (g, h, i)  
997 Distribution of OMNI  $B_x$ ,  $B_y$ ,  $B_z$  when the agreement of  $n_{CIS}$  is poor. (j, k, l) Distribution of  
998 OMNI  $B_x$ ,  $B_y$ ,  $B_z$  when the agreement of  $n_{EFW}$  is poor. The values are in percentage unit in  
999 the distributions.



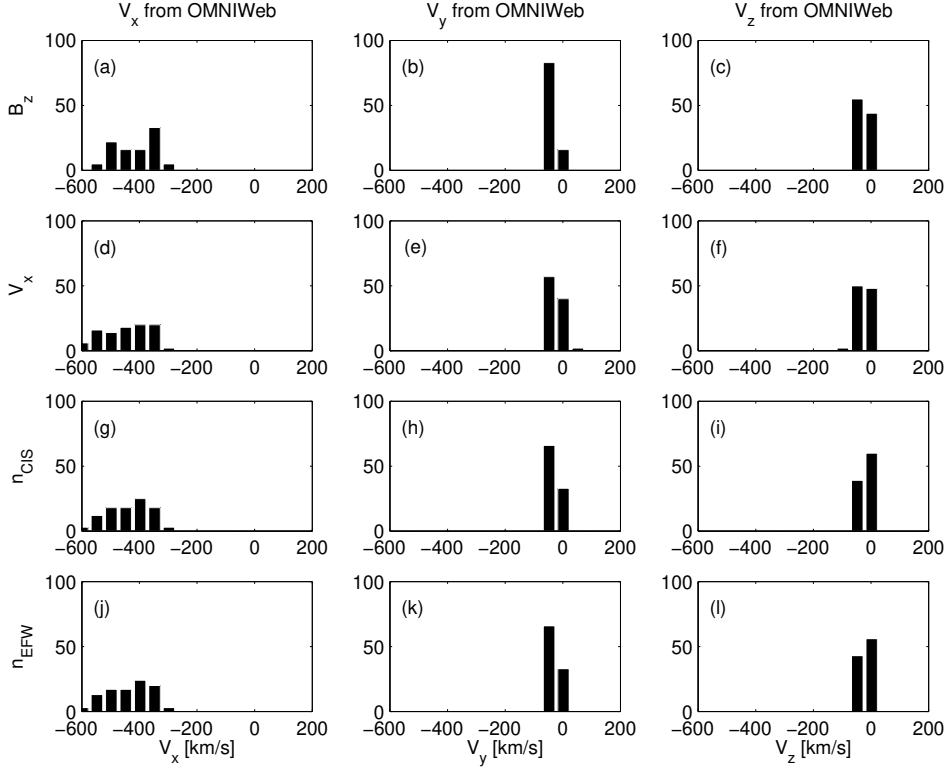
1000 **Figure 15.** The distributions of the  $V_x$ , the  $V_y$  and the  $V_z$  OMNI solar wind magnetic field  
 1001 components when the agreement of the Cluster SC3 measurements and the GUMICS–4 simu-  
 1002 lations are poor in the solar wind (see Table 4). The  $B_z$ , the  $V_x$ , the  $n_{CIS}$  and the  $n_{EFW}$  are  
 1003 the magnetic field GSE Z component, the plasma ion velocity X GSE component, the solar wind  
 1004 density measured by the CIS HIA instrument and the calculated from the EFW spacecraft po-  
 1005 tential, respectively. (a, b, c) Distribution of OMNI  $V_x$ ,  $V_y$ ,  $V_z$  when the agreement of  $B_z$  is poor.  
 1006 (d, e, f) Distribution of OMNI  $V_x$ ,  $V_y$ ,  $V_z$  when the agreement of  $V_x$  is poor. (g, h, i) Distribution  
 1007 of OMNI  $V_x$ ,  $V_y$ ,  $V_z$  when the agreement of  $n_{CIS}$  is poor. (j, k, l) Distribution of OMNI  $V_x$ ,  $V_y$ ,  
 1008  $V_z$  when the agreement of  $n_{EFW}$  is poor. The values are in percentage unit in the distributions.



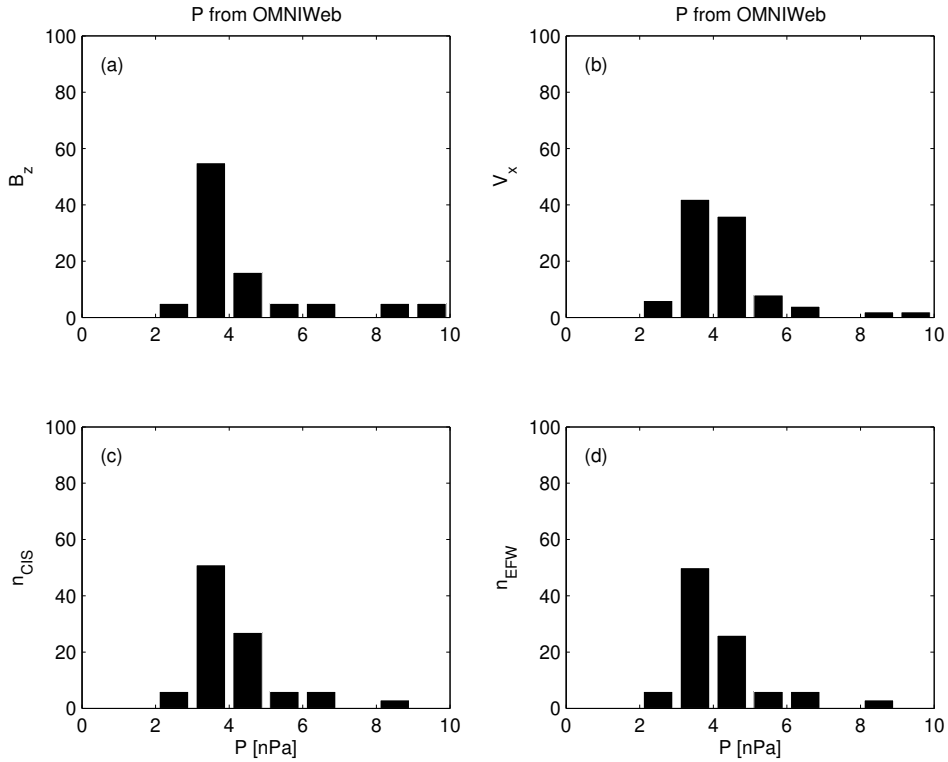
1009      **Figure 16.** The distributions of the  $P$  solar wind dynamic pressure calculated from OMNI  
 1010 parameters when the agreement of the Cluster SC3 measurements and the GUMICS–4 simula-  
 1011 tions are poor in the solar wind (see Table 4). The  $B_z$ ,  $V_x$ ,  $n_{CIS}$  and  $n_{EFW}$  are the magnetic  
 1012 field GSE Z component, the velocity X GSE component, the solar wind density measured by the  
 1013 CIS HIA instrument and calculated from the EFW spacecraft potential, respectively. (a, b, c, d)  
 1014 The distribution of the  $P$  calculated from OMNI data when the agreement of the  $B_z$ , the  $V_x$ , the  
 1015  $n_{CIS}$  or the  $n_{EFW}$  are poor. The values are in percentage unit in the distributions.



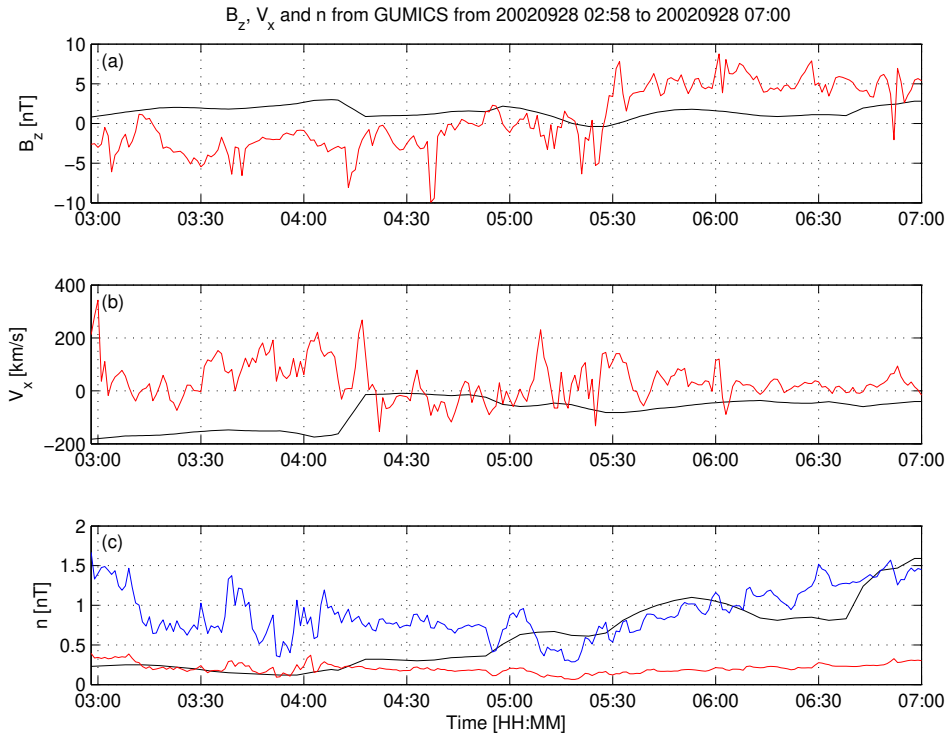
1016      **Figure 17.** The distributions of the  $B_x$ , the  $B_y$  and the  $B_z$  OMNI solar wind magnetic field  
 1017      components when the agreement of the Cluster SC3 measurements and the GUMICS–4 simu-  
 1018      lations are poor in the magnetosheath (see Table 5). The  $B_z$ , the  $V_x$ , the  $n_{CIS}$  and the  $n_{EFW}$   
 1019      are the magnetic field GSE Z component, the plasma ion velocity X GSE component, the solar  
 1020      wind density measured by the CIS HIA instrument and the calculated from the EFW spacecraf-  
 1021      t potential, respectively. (a, b, c) Distribution of OMNI  $B_x$ ,  $B_y$ ,  $B_z$  when the agreement of  $B_z$   
 1022      is poor. (d, e, f) Distribution of OMNI  $B_x$ ,  $B_y$ ,  $B_z$  when the agreement of  $V_x$  is poor. (g, h, i)  
 1023      Distribution of OMNI  $B_x$ ,  $B_y$ ,  $B_z$  when the agreement of  $n_{CIS}$  is poor. (j, k, l) Distribution of  
 1024      OMNI  $B_x$ ,  $B_y$ ,  $B_z$  when the agreement of  $n_{EFW}$  is poor. The values are in percentage unit in  
 1025      the distributions.



1026 **Figure 18.** The distributions of the  $V_x$ , the  $V_y$  and the  $V_z$  OMNI solar wind magnetic field  
 1027 components when the agreement of the Cluster SC3 measurements and the GUMICS–4 simula-  
 1028 tions are poor in the magnetosheath (see Table 5). The  $B_z$ , the  $V_x$ , the  $n_{CIS}$  and the  $n_{EFW}$  are  
 1029 the magnetic field GSE Z component, the plasma ion velocity X GSE component, the solar wind  
 1030 density measured by the CIS HIA instrument and the calculated from the EFW spacecraft po-  
 1031 tential, respectively. (a, b, c) Distribution of OMNI  $V_x$ ,  $V_y$ ,  $V_z$  when the agreement of  $B_z$  is poor.  
 1032 (d, e, f) Distribution of OMNI  $V_x$ ,  $V_y$ ,  $V_z$  when the agreement of  $V_x$  is poor. (g, h, i) Distribution  
 1033 of OMNI  $V_x$ ,  $V_y$ ,  $V_z$  when the agreement of  $n_{CIS}$  is poor. (j, k, l) Distribution of OMNI  $V_x$ ,  $V_y$ ,  
 1034  $V_z$  when the agreement of  $n_{EFW}$  is poor. The values are in percentage unit in the distributions.



1035      **Figure 19.** The distributions of the  $P$  solar wind dynamic pressure calculated from OMNI pa-  
 1036      rameters when the agreement of the Cluster SC3 measurements and the GUMICS-4 simulations  
 1037      are poor in the magnetosheath (see Table 5). The  $B_z$ ,  $V_x$ ,  $n_{CIS}$  and  $n_{EFW}$  are the magnetic  
 1038      field GSE Z component, the velocity X GSE component, the solar wind density measured by the  
 1039      CIS HIA instrument and calculated from the EFW spacecraft potential, respectively. (a, b, c, d)  
 1040      The distribution of the  $P$  calculated from OMNI data when the agreement of the  $B_z$ , the  $V_x$ , the  
 1041       $n_{CIS}$  or the  $n_{EFW}$  are poor. The values are in percentage unit in the distributions.



1042      **Figure 20.** GUMICS-4 simulation results (black) and Cluster SC3 magnetic field Z compo-  
 1043      nent, ion plasma moments (red) and electron density calculated from spacecraft potential (blue)  
 1044      from September 28, 2002 from 2:58 to 7:00 (UT) in the tail in GSE system. (a) Magnetic field  
 1045      Z component. (b) Solar wind velocity X component (c) Solar wind density. From 05:15 to 05:30  
 1046      both the Cluster SC3 and the virtual spaceprobe of the GUMICS-4 simulation cross the neutral  
 1047      sheet multiple times.

Start/End	$C_{B_z}$	$\delta t_{B_z}$	$C_{V_x}$	$\delta t_{V_x}$	$C_{n_{CIS}}$	$\delta t_{n_{CIS}}$	$C_{n_{EFW}}$	$\delta t_{n_{EFW}}$
	[min]		[min]		[min]		[min]	
20020201 20:00/0203 04:00	0.96	2	1.00	13	0.96	3	0.98	3
20020211 13:00/0212 12:00	0.82	2	1.00	0	0.99	18	0.99	18
20020218 09:00/0219 02:00	0.93	0	1.00	-3	0.94	-3	0.97	-3
20020219 06:30/0219 15:00	0.93	1	1.00	0	0.99	-60	1.00	-52
20020220 18:30/0222 00:00	0.87	4	1.00	4	0.93	-21	0.98	3
20020318 17:30/0319 02:30	0.89	1	1.00	21	0.98	50	0.99	5
20020412 20:30/0413 02:00	0.90	4	0.99	-54	0.94	60	0.98	12
20021227 12:00/1228 03:00	0.75	4	1.00	-3	0.99	-26	0.99	21
20021229 20:00/1230 16:00	0.68	1	1.00	1	0.99	-30	0.98	41
20030106 06:00/0106 19:00	0.79	4	1.00	6	0.99	4	0.99	-60
20030108 07:00/0109 03:30	0.55	10	1.00	41	0.99	10	0.97	-55
20030113 08:30/0113 18:00	0.91	3	1.00	5	1.00	3	0.97	-1
20030120 07:30/0120 13:00	0.82	2	1.00	9	1.00	-6	1.00	-3
20030122 12:00/0123 14:00	0.81	2	1.00	3	0.99	3	0.92	-60
20030124 18:00/0126 00:00	0.73	3	1.00	0	0.99	-60	0.99	60
20030127 16:00/0128 06:00	0.88	-1	1.00	-3	0.95	1	0.88	11
20030129 12:00/0130 18:00	0.90	2	1.00	4	0.94	-59	0.98	1

1048 **Table 1.** The studied solar wind intervals. The correlation coefficients ( $C_{B_z}$ ,  $C_{V_x}$ ,  $C_{n_{CIS}}$ ,  
1049  $C_{n_{EFW}}$ ) and time shift ( $\delta t_{V_x}$ ,  $\delta t_{n_{CIS}}$ ,  $\delta t_{n_{EFW}}$ ) in minutes of the magnetic field GSE Z compo-  
1050 nent ( $B_z$ ), solar wind velocity X component ( $V_x$ ), CIS and EFW densities ( $n_{CIS}$ ,  $n_{EFW}$ ).

Table 2: The studied magnetosheath intervals. The correlation coefficients ( $C_{B_z}$ ,  $C_{V_x}$ ,  $C_{n_{CIS}}$ ,  $C_{n_{EFW}}$ ) and time shift ( $\delta t_{V_x}$ ,  $\delta t_{n_{CIS}}$ ,  $\delta t_{n_{EFW}}$ ) in minutes of the magnetic field GSE Z component ( $B_z$ ), solar wind velocity X component ( $V_x$ ), CIS and EFW densities ( $n_{CIS}$ ,  $n_{EFW}$ ). In the empty slots the correlation calculation gives invalid result.

Start/End	$C_{B_z}$	$\delta t_{B_z}$	$C_{V_x}$	$\delta t_{V_x}$	$C_{n_{CIS}}$	$\delta t_{n_{CIS}}$	$C_{n_{EFW}}$	$\delta t_{n_{EFW}}$
		[min]		[min]		[min]		[min]
20020201 13:30/0201 18:30	0.91	1	0.98	56	0.99	60	0.976	60
20020208 18:15/0209 00:00	0.73	2	0.95	60	0.98	-52	0.98	-54
20020211 02:30/0211 09:00	0.79	0	0.99	-20	0.99	-1	0.99	1
20020212 16:30/0212 21:00	0.80	3	0.99	54	0.99	31	0.99	30
20020219 17:30/0219 23:00	0.76	4	0.98	37	0.99	7	0.99	6
20020222 23:00/0223 06:30	0.64	0	0.97	-60	0.99	-47	0.98	-48
20020227 16:30/0227 23:15	0.48	59	0.98	-31	0.99	-39	1.00	-12
20020310 18:30/0311 00:30	0.97	3	0.98	19	0.99	8	0.99	-2
20020311 14:00/0311 19:00	0.86	5	0.97	36	0.99	-3	0.99	-40
20020406 19:00/0407 01:15	0.76	2	0.96	-60	0.98	-55	0.98	-56
20020410 17:30/0410 23:00	0.89	6	0.99	-50	0.99	3	1.00	5
20020411 11:30/0411 16:30	0.82	4	0.99	39	0.99	3	0.99	3
20020418 18:30/0418 22:45	0.92	60	0.99	-60	0.99	60	0.98	60
20020421 04:30/0421 07:45	0.96	47	0.99	-60	1.00	-60	1.00	-60
20020422 11:45/0422 15:45	0.73	-5	0.98	-17	0.99	-15	0.98	-16
20020423 08:30/0423 12:30	0.93	31	0.99	3	0.99	16	0.99	16
20020430 12:30/0430 17:00	0.79	59	0.98	22	0.98	-18		
20020505 07:00/0505 11:15	0.71	59	0.99	-58	0.98	-60		
20020506 19:15/0507 00:15	0.84	-27	0.98	-60	0.97	-37		
20020507 17:30/0507 23:00	0.93	2	0.98	-30	0.99	-49		
20020514 22:45/0515 03:00	0.79	49	0.99	35	0.99	38	0.99	43
20020517 07:00/0517 12:15	0.74	-5	1.00	-5	0.99	-4	0.99	-3
20020518 13:30/0518 19:30	0.70	1	0.99	9	0.97	-1	0.97	-1

*Continued on next page*

Table 2 – *Continued from previous page*

Start/End	$C_{B_z}$	$\delta t_{B_z}$	$C_{V_x}$	$\delta t_{V_x}$	$C_{n_{CIS}}$	$\delta t_{n_{CIS}}$	$C_{n_{EFW}}$	$\delta t_{n_{EFW}}$
		[min]		[min]		[min]		[min]
20020519 20:00/0520 03:30	0.98	2	1.00	-9	0.99	-5	0.99	-50
20020520 10:45/0520 20:15	0.77	1	0.99	-3	0.95	-1	0.99	-1
20020522 02:00/0522 08:45	0.49	52	0.99	4	0.99	12	0.99	22
20020527 02:15/0527 17:15	0.79	-3	0.99	-3	0.98	0	0.98	0
20020530 05:00/0530 10:30	0.29	3	1.00	-38	0.99	3	0.99	3
20020601 19:30/0602 01:00	0.68	-2	1.00	18	0.99	-6	0.99	-7
20020602 21:45/0603 17:45	0.62	-5	0.99	-1	0.98	2	0.99	2
20020605 10:30/0606 06:00	0.18	0	1.00	-7	0.97	10	0.98	9
20020607 18:00/0607 22:00	0.92	-35	1.00	-36	0.99	16	0.99	16
20020608 01:15/0608 18:15	0.53	-4	0.99	-39	0.96	-6	0.97	-6
20020610 01:30/0610 09:30	0.76	5	0.99	8	0.99	-5	0.99	-7
20020610 11:00/0611 01:00	0.87	-4	0.99	-33	0.98	23	0.99	6
20020612 18:30/0613 06:15	0.44	-2	0.99	-7	0.97	4	0.97	-32
20020615 07:00/0615 23:30			1.00	47	0.98	-3	0.98	-3
20020617 05:00/0618 03:45	0.76	4	1.00	28	0.98	10	0.98	8
20020620 04:00/0620 11:00	0.61	-8	0.99	-6	0.97	12	0.98	4
20020622 14:30/0622 18:00	0.98	55	1.00	35	0.99	16	1.00	16
20021201 04:15/1202 07:45	0.38	1	1.00	2	0.99	6	0.99	6
20021203 15:30/1204 19:30	0.67	1	0.99	60	0.98	59	0.98	59
20021207 00:30/1207 07:45	0.49	37	0.98	-56	0.99	-19	0.99	-4
20021208 09:30/1209 08:00	0.69	2	0.98	-35	0.97	6	0.98	4
20021212 23:30/1213 14:30	0.51	5	1.00	36	0.99	-3	0.81	-56
20021213 21:15/1214 09:30	0.93	5	0.99	-35	0.99	-13	0.99	-47
20021215 12:45/1216 18:00	0.76	2	0.99	-60	0.94	-60	0.98	31
20021217 16:30/1218 01:45	0.99	2	1.00	-54	0.99	3	0.99	3
20021220 01:30/1220 06:15	0.92	0	1.00	60	0.99	2	0.99	3
20021223 02:15/1223 13:00	0.91	1	0.97	49	0.93	49	0.99	-14
20021223 14:00/1223 22:30	0.84	1	0.99	-2	0.99	-1	1.00	-3
20021224 19:00/1225 01:45	0.94	0	1.00	-44	0.99	26	0.99	27

*Continued on next page*

Table 2 – *Continued from previous page*

Start/End	$C_{B_z}$	$\delta t_{B_z}$	$C_{V_x}$	$\delta t_{V_x}$	$C_{n_{CIS}}$	$\delta t_{n_{CIS}}$	$C_{n_{EFW}}$	$\delta t_{n_{EFW}}$
		[min]		[min]		[min]		[min]
20021225 23:45/1226 07:15	0.96	7	1.00	-17	0.99	56	0.99	55
20021226 23:00/1227 09:45	0.79	2	1.00	2	0.98	4	0.99	3
20021229 11:45/1229 17:00	0.60	2	1.00	-60	0.98	-19	0.98	50
20021230 17:45/1231 01:00	0.69	1	0.98	52	0.98	60	0.98	22
20021231 23:00/0101 05:15	0.89	2	0.99	15	0.99	-54	1.00	-58
20030105 14:00/0105 21:00	0.69	0	0.99	1	0.98	-60	0.99	-60
20030106 23:15/0107 03:00	0.52	9	0.98	60	0.99	56	1.00	-60
20030109 08:45/0109 16:15			0.91	-56	0.98	-13	0.98	-26
20030110 07:15/0110 15:15	0.94	1	0.99	-7	0.99	1	0.98	5
20030111 08:15/0111 22:30	0.84	0	0.99	-59	0.94	-15	0.94	8
20030112 17:30/0113 00:15	0.98	0	1.00	-52	0.99	39	0.99	51
20030114 00:30/0114 08:30	0.84	-1	0.99	-60	0.98	23	0.98	8
20030116 10:15/0116 17:45	0.62	60	0.93	52	0.99	60	0.99	30
20030117 09:30/0117 13:30	0.68	-3	1.00	8	1.00	-31	0.99	-33
20030118 23:30/0119 03:45	0.93	3	1.00	-12	1.00	7	0.99	7
20030119 21:00/0120 01:00	0.94	3	1.00	5	1.00	38	1.00	19
20030121 06:30/0121 11:30	0.82	-15	0.96	47	0.98	7	0.99	-39
20030122 04:45/0122 09:30	0.69	-2	1.00	10	0.99	-9	0.99	-5
20030126 01:45/0126 06:30	0.85	3	0.99	-15	0.99	-50	0.99	23
20030127 08:15/0127 13:00	1.00	9	1.00	-60	0.98	0	0.99	1
20030128 12:30/0128 17:15	0.77	60	0.99	-24	0.99	-6	0.988	20
20030130 19:45/0131 00:15	0.98	2	0.99	51	0.99	25	0.99	9

Table 3: The studied magnetosphere intervals (UT).

Start/End
20020213 23:00/0214 01:30
20020217 18:30/0218 02:00
20020220 00:45/0220 12:00
20020222 11:15/0222 20:15
20020225 02:15/0225 08:30
20020227 06:00/0227 12:00
20020302 00:00/0302 03:15
20020306 10:00/0306 18:30
20020308 17:30/0309 06:00
20020311 02:15/0311 12:00
20020313 11:15/0314 00:15
20020316 04:45/0316 08:00
20020318 09:00/0318 14:45
20020320 20:30/0320 23:55
20020323 04:00/0323 09:45
20020327 23:45/0328 06:15
20020330 07:15/0330 12:45
20020401 19:30/0401 22:00
20020406 09:30/0406 18:00
20020408 15:00/0409 00:00
20020410 23:30/0411 09:45
20020413 08:30/0413 19:00
20020416 18:00/0417 04:30
20020418 06:00/0418 12:00
20020420 15:00/0420 23:00
20020422 20:00/0423 07:00
20020425 08:30/0425 18:00
20020430 04:40/0430 12:00
20020504 14:30/0504 16:45

*Continued on next page*

Table 3 – *Continued from previous page*

Start/End
20020505 02:30/0505 07:00
20020507 01:30/0507 15:45
20020508 11:00/0510 04:15
20020512 02:45/0512 09:30
20020514 10:30/0514 12:45
20020519 00:30/0519 19:30
20020521 01:30/0521 22:00
20020523 23:30/0524 02:00
20020524 19:00/0525 08:15
20020526 07:30/0526 10:30
20020528 20:00/0529 05:00
20020531 02:15/0531 13:30
20020602 04:30/0602 07:30
20020602 12:00/0602 21:30
20020604 08:30/0605 07:00
20020606 14:30/0607 16:30
20020609 06:00/0609 20:00
20020611 11:00/0612 13:00
20020614 01:00/0614 16:00
20020616 08:00/0616 18:00
20020620 13:30/0622 01:00
20020623 13:00/0623 17:00
20020624 04:00/0624 10:15
20020630 17:45/0701 15:00
20020701 21:00/0703 10:30
20020703 23:00/0706 03:15
20020707 01:00/0708 23:00
20020710 11:30/0714 03:30
20020714 15:45/0715 15:30
20020716 23:30/0717 16:00

*Continued on next page*

Table 3 – *Continued from previous page*

Start/End
20020718 05:45/0722 11:00
20020722 23:45/0728 01:00
20020728 02:00/0804 03:45
20020804 04:45/0811 06:15
20020811 07:30/0816 01:00
20020816 15:30/0818 09:00
20020818 10:00/0825 11:30
20020825 13:00/0901 14:15
20020901 17:15/0903 23:30
20020905 02:15/0906 16:30
20020907 10:30/0908 17:00
20020908 18:00/0915 19:30
20020915 21:00/0922 22:30
20020923 00:00/0923 23:30
20020924 03:30/0928 22:45
20020928 23:30/0930 01:00
20020930 02:15/1006 17:00
20021006 17:45/1007 03:30
20021007 05:00/1007 17:30
20021008 07:30/1010 22:00
20021010 22:30/1012 22:30
20021012 23:00/1014 06:30
20021014 09:00/1016 04:00
20021016 14:00/1019 00:15
20021019 01:30/1019 22:00
20021021 04:00/1022 19:30
20021022 22:30/1026 02:30
20021026 04:00/1029 20:15
20021030 01:30/1102 08:00
20021102 22:00/1104 22:00

*Continued on next page*

Table 3 – *Continued from previous page*

Start/End
20021106 00:00/1107 18:00
20021108 02:00/1109 18:45
20021111 00:00/1112 01:30
20021113 03:45/1114 14:15
20021115 20:30/1116 23:00
20021118 01:00/1118 23:30
20021120 17:00/1121 06:00
20021122 21:30/1124 01:00
20021125 04:00/1126 08:30
20021127 20:00/1128 18:30
20021130 04:00/1201 01:30
20021202 14:30/1203 09:00
20021204 22:00/1205 19:30
20021207 09:00/1207 16:30
20021207 18:00/1207 22:00
20021209 16:30/1210 14:30
20021212 13:45/1212 21:30
20021214 13:30/1214 20:00
20021214 21:00/1215 07:30
20021216 21:00/1217 15:00
20021219 08:00/1219 19:30
20021221 15:45/1221 23:15
20021222 00:30/1222 08:45
20021224 02:30/1224 14:00
20021226 10:00/1226 19:00
20021228 19:30/1229 02:30
20021229 04:00/1229 10:00
20021231 05:00/1231 18:45
20030102 12:30/0102 20:45
20030104 20:45/0105 06:00

*Continued on next page*

Table 3 – *Continued from previous page*

Start/End
20030105 07:00/0105 13:30
20030107 05:45/0107 21:00
20030109 17:00/0110 00:45
20030112 00:00/0112 09:15
20030112 10:30/0112 16:00
20030114 11:00/0114 20:00
20030116 20:30/0116 22:45
20030119 04:30/0119 09:30
20030119 14:00/0119 17:00
20030121 13:30/0121 21:30
20030126 07:30/0126 15:45
20030128 17:45/0129 08:15
20030131 01:30/0131 11:45

Start/End	OMNI			Cluster SC3			
	$B_z$ [nT]	$V_x$ [km/s]	P [cm $^{-3}$ ]	$B_z$	$V_x$	$n_{CIS}$	$n_{EFW}$
20020201 20:00/0203 04:00	-1.25	-373.52	4.08	y	y	n	y
20020211 13:00/0212 12:00	0.03	-533.11	2.18	y	y	y	y
20020218 09:00/0219 02:00	2.56	-362.41	3.46	y	n	n	y
20020219 06:30/0219 15:00	3.55	-401.63	1.25	y	y	n	n
20020220 18:30/0222 00:00	1.95	-440.18	1.96	y	y	n	y
20020318 17:30/0319 02:30	3.79	-429.30	15.34	y	n	n	n
20020412 20:30/0413 02:00	-1.81	-420.35	3.24	y	n	n	y
20021227 12:00/1228 03:00	0.09	-714.40	2.72	y	n	n	y
20021229 20:00/1230 16:00	-0.37	-526.40	2.26	y	y	n	n
20030106 06:00/0106 19:00	2.25	-399.91	1.50	y	n	n	n
20030108 07:00/0109 03:30	-0.58	-280.80	2.97	n	n	y	n
20030113 08:30/0113 18:00	0.68	-397.83	1.72	y	y	y	n
20030120 07:30/0120 13:00	2.16	-630.69	2.43	y	y	y	y
20030122 12:00/0123 14:00	0.13	-608.96	3.41	y	y	y	n
20030124 18:00/0126 00:00	-0.71	-739.68	2.87	y	y	n	n
20030127 16:00/0128 06:00	-0.92	-451.84	3.12	y	y	n	n
20030129 12:00/0130 18:00	-3.09	-450.00	3.96	y	y	n	y

1053 **Table 4.** The average OMNI input parameters in the solar wind and the good/bad agreement  
 1054 of the GUMICS–4 simulations to the Cluster  $B_z$  magnetic field component, the  $V_x$  solar wind  
 1055 speed component, the  $n_{CIS}$  solar wind density measured by the Cluster CIS HIA instrument and  
 1056 the  $n_{EFW}$  solar wind density calculated from the spacecraft potential measured by the Cluster  
 1057 EFW instrument in the solar wind.

Table 5: The average OMNI input parameters in the solar wind and the good/bad agreement of the GUMICS–4 simulations to the Cluster  $B_z$  magnetic field component, the  $V_x$  solar wind speed component, the  $n_{CIS}$  solar wind density measured by the Cluster CIS HIA instrument and the  $n_{EFW}$  solar wind density calculated from the spacecraft potential measured by the Cluster EFW instrument in the magnetosheath.

Start/End	OMNI			Cluster SC3			
	$B_z$	$V_x$	P	$B_z$	$V_x$	$n_{CIS}$	$n_{EFW}$
	[nT]	[km/s]	[cm $^{-3}$ ]				
20020201 13:30/0201 18:30	0.19	-342.87	4.62	y	n	n	n
20020208 18:15/0209 00:00	-0.48	-508.16	1.61	y	n	n	n
20020211 02:30/0211 09:00	-1.85	-425.67	1.78	y	y	y	y
20020212 16:30/0212 21:00	2.98	-509.22	2.34	y	n	n	n
20020219 17:30/0219 23:00	1.46	-431.50	1.46	y	y	y	y
20020222 23:00/0223 06:30	0.86	-391.22	1.14	y	n	n	n
20020227 16:30/0227 23:15	1.89	-343.13	1.52	n	n	n	n
20020310 18:30/0311 00:30	-2.81	-379.46	1.78	y	y	y	y
20020311 14:00/0311 19:00	1.63	-371.43	2.68	n	n	n	n
20020406 19:00/0407 01:15	-2.71	-333.13	0.93	y	n	n	n
20020410 17:30/0410 23:00	0.31	-312.43	4.42	n	n	y	y
20020411 11:30/0411 16:30	-1.50	-494.02	4.25	y	y	n	n
20020418 18:30/0418 22:45	-0.92	-450.82	0.30	n	n	n	n
20020421 04:30/0421 07:45	0.40	-455.69	1.37	n	n	n	n
20020422 11:45/0422 15:45	0.25	-419.98	1.14	n	n	y	y
20020423 08:30/0423 12:30	2.77	-507.99	6.82	n	n	n	n
20020430 12:30/0430 17:00	2.15	-479.51	3.02	n	n	n	n
20020505 07:00/0505 11:15	0.20	-336.81	1.74	n	n	n	n
20020506 19:15/0507 00:15	0.78	-390.00	2.46	y	n	n	n
20020507 17:30/0507 23:00	2.87	-392.40	3.49	y	n	n	n
20020514 22:45/0515 03:00	-2.42	-414.01	1.82	n	n	n	n

*Continued on next page*

Table 5 – *Continued from previous page*

Start/End	OMNI			Cluster SC3			
	$B_z$ [nT]	$V_x$ [km/s]	P $[cm^{-3}]$	$B_z$	$V_x$	$n_{CIS}$	$n_{EFW}$
20020517 07:00/0517 12:15	-0.39	-379.32	1.52	y	y	y	y
20020518 13:30/0518 19:30	0.63	-345.87	1.59	n	n	y	y
20020519 20:00/0520 03:30	4.75	-408.56	1.12	y	y	y	y
20020520 10:45/0520 20:15	0.74	-448.89	1.93	y	y	y	y
20020522 02:00/0522 08:45	-1.07	-398.12	1.63	n	y	y	y
20020527 02:15/0527 17:15	-3.11	-542.53	2.07	y	y	y	y
20020530 05:00/0530 10:30	0.03	-493.86	2.08	y	n	y	y
20020601 19:30/0602 01:00	-3.38	-342.27	4.16	y	y	y	y
20020602 21:45/0603 17:45	0.38	-435.47	1.89	y	y	y	y
20020605 10:30/0606 06:00	-0.42	-394.49	1.08	y	y	n	n
20020607 18:00/0607 22:00	-1.60	-291.85	1.80	y	y	y	y
20020608 01:15/0608 18:15	0.06	-335.39	2.74	y	n	y	y
20020610 01:30/0610 09:30	1.60	-465.52	3.00	y	y	y	y
20020610 11:00/0611 01:00	-2.27	-419.86	2.16	y	n	y	y
20020612 18:30/0613 06:15	-1.13	-351.03	1.16	y	y	y	y
20020615 07:00/0615 23:30	-1.16	-334.27	2.84	n	n	y	y
20020617 05:00/0618 03:45	0.78	-351.47	1.87	y	n	y	y
20020620 04:00/0620 11:00	0.46	-485.48	1.73	y	y	y	y
20020622 14:30/0622 18:00	-0.72	-429.02	1.93	n	n	y	y
20021201 04:15/1202 07:45	-1.09	-499.23	2.62	y	y	y	y
20021203 15:30/1204 19:30	0.34	-449.09	2.06	y	n	n	n
20021207 00:30/1207 07:45	0.80	-451.80	7.33	n	n	y	y
20021208 09:30/1209 08:00	0.60	-600.27	1.49	y	n	y	y
20021212 23:30/1213 14:30	0.10	-337.77	1.32	y	n	n	n
20021213 21:15/1214 09:30	-0.74	-361.19	2.99	y	n	y	y
20021215 12:45/1216 18:00	1.32	-479.48	1.53	y	n	n	n
20021217 16:30/1218 01:45	4.56	-393.99	2.49	y	n	y	y
20021220 01:30/1220 06:15	-1.21	-530.62	3.01	y	n	y	y

*Continued on next page*

Table 5 – *Continued from previous page*

Start/End	OMNI			Cluster SC3			
	$B_z$ [nT]	$V_x$ [km/s]	P $[cm^{-3}]$	$B_z$	$V_x$	$n_{CIS}$	$n_{EFW}$
20021223 02:15/1223 13:00	-2.32	-516.12	2.22	y	n	n	n
20021223 14:00/1223 22:30	0.89	-519.77	2.55	y	y	y	y
20021224 19:00/1225 01:45	0.88	-523.86	3.41	y	n	y	y
20021225 23:45/1226 07:15	-0.61	-414.38	2.21	y	y	n	n
20021226 23:00/1227 09:45	-1.79	-618.14	6.20	y	y	y	y
20021229 11:45/1229 17:00	-0.41	-580.12	2.39	y	n	n	n
20021230 17:45/1231 01:00	-1.01	-483.60	1.93	y	n	n	y
20021231 23:00/0101 05:15	0.60	-418.95	1.94	y	n	n	n
20030105 14:00/0105 21:00	-0.03	-414.46	1.69	y	n	n	n
20030106 23:15/0107 03:00	-1.62	-392.29	1.56	n	n	n	n
20030109 08:45/0109 16:15	1.45	-272.82	2.31	n	n	n	n
20030110 07:15/0110 15:15	-2.11	-401.03	2.72	y	n	y	y
20030111 08:15/0111 22:30	-0.20	-433.33	1.24	y	n	n	y
20030112 17:30/0113 00:15	1.53	-389.62	1.45	y	n	n	n
20030114 00:30/0114 08:30	-1.67	-388.53	2.27	y	n	n	y
20030116 10:15/0116 17:45	-1.20	-328.91	1.22	n	n	n	n
20030117 09:30/0117 13:30	-1.36	-327.09	2.55	y	y	y	y
20030118 23:30/0119 03:45	6.41	-459.46	4.82	y	y	y	y
20030119 21:00/0120 01:00	1.52	-597.95	2.38	y	n	y	y
20030121 06:30/0121 11:30	-1.77	-670.25	1.50	y	n	n	n
20030122 04:45/0122 09:30	0.11	-588.87	2.30	y	n	y	y
20030126 01:45/0126 06:30	-0.24	-713.82	2.75	y	y	y	y
20030127 08:15/0127 13:00	7.94	-509.30	0.47	y	n	y	y
20030128 12:30/0128 17:15	4.95	-443.83	4.15	y	y	y	y
20030130 19:45/0131 00:15	4.21	-510.33	2.63	y	n	y	y

Table 6: Intervals around the studied bow shock crossings. The Cluster SC3 crossed the bow shock in all cases. The 2nd column shows whether the bow shock is visible in the GUMICS–4 simulations.

Start/End	GUMICS Bow Shock
20020201 12:00/0202 00:00	+
20020203 00:00/0203 12:00	+
20020206 06:00/0206 18:00	+
20020208 18:00/0209 06:00	+
20020211 06:00/0211 18:00	+
20020212 12:00/0212 18:00	+
20020213 12:00/0213 18:00	+
20020216 00:00/0216 12:00	+
20020217 06:00/0217 12:00	-
20020218 06:00/0218 18:00	+
20020219 00:00/0219 18:00	+
20020220 12:00/0221 00:00	+
20020221 18:00/0222 00:00	+
20020301 06:00/0301 12:00	+
20020304 12:00/0304 18:00	+
20020306 00:00/0306 06:00	+
20020307 00:00/0307 06:00	+
20020308 06:00/0308 12:00	+
20020309 06:00/0309 12:00	+
20020310 12:00/0311 00:00	+
20020311 18:00/0312 00:00	+
20020313 00:00/0313 06:00	-
20020314 00:00/0314 12:00	+
20020316 06:00/0316 18:00	+
20020318 12:00/0319 00:00	+
20020323 12:00/0323 18:00	+

*Continued on next page*

Table 6 – *Continued from previous page*

Start/End	GUMICS Bow Shock
20020325 18:00/0326 06:00	–
20020327 06:00/0327 12:00	+
20020329 18:00/0330 00:00	–
20020402 00:00/0402 06:00	+
20020405 18:00/0406 00:00	–
20020407 00:00/0407 06:00	–
20020409 06:00/0409 12:00	–
20020410 12:00/0410 18:00	–
20020411 12:00/0411 18:00	–
20020413 00:00/0413 06:00	+
20020413 18:00/0414 06:00	+
20020420 00:00/0420 06:00	+
20020423 12:00/0423 23:00	+
20020427 00:00/0427 06:00	+
20020428 06:00/0428 12:00	+
20020430 18:00/0501 00:00	+
20020505 06:00/0505 18:00	–
20020507 18:00/0509 06:00	+
20020510 06:00/0510 12:00	+
20020513 12:00/0513 18:00	+
20020515 00:00/0515 06:00	–
20020520 00:00/0520 06:00	+
20020522 06:00/0522 12:00	+
20020522 18:00/0523 06:00	+
20021206 06:00/1207 06:00	+
20021218 00:00/1219 00:00	+
20021220 18:00/1221 00:00	+
20021221 00:00/1221 12:00	+
20021222 12:00/1223 00:00	+
20021223 00:00/1223 06:00	+

*Continued on next page*

Table 6 – *Continued from previous page*

Start/End	GUMICS Bow Shock
20021225 06:00/1226 00:00	+
20021227 06:00/1228 00:00	+
20021228 00:00/1228 12:00	+
20021229 12:00/1230 00:00	+
20030101 06:00/0102 00:00	+
20030103 06:00/0103 12:00	+
20030104 00:00/0104 18:00	+
20030106 00:00/0107 00:00	+
20030108 00:00/0108 12:00	+
20030113 00:00/0114 06:00	+
20030115 00:00/0115 12:00	+
20030118 18:00/0119 00:00	+
20030120 00:00/0121 12:00	+
20030122 06:00/0122 12:00	+
20030123 12:00/0124 00:00	+
20030124 12:00/0124 18:00	+
20030126 00:00/0126 06:00	+
20030127 00:00/0127 18:00	+
20030128 06:00/0128 18:00	+
20030129 06:00/0129 12:00	+
20030130 18:00/0131 00:00	+

Table 7: Intervals around the studied magnetopause crossings.  
The Cluster SC3 crossed the magnetopause in all cases. The  
2nd column shows whether the magnetopause is visible in the  
GUMICS–4 simulations.

Start/End	GUMICS Magnetopause
20020203 06:00/0203 12:00	+
20020206 06:00/0206 12:00	-
20020211 00:00/0211 06:00	+
20020218 00:00/0218 06:00	+
20020225 06:00/0225 12:00	+
20020302 00:00/0302 06:00	+
20020306 18:00/0307 00:00	-
20020308 12:00/0308 18:00	-
20020311 12:00/0311 18:00	+
20020313 18:00/0314 00:00	-
20020314 00:00/0314 06:00	+
20020323 06:00/0323 12:00	+
20020330 12:00/0330 18:00	-
20020404 06:00/0404 12:00	-
20020409 00:00/0409 06:00	-
20020418 12:00/0418 18:00	+
20020422 12:00/0422 18:00	-
20020429 18:00/0430 00:00	-
20020507 12:00/0507 18:00	-
20020509 06:00/0509 12:00	-
20020510 00:00/0510 06:00	-
20020514 18:00/0515 00:00	-
20020519 12:00/0519 18:00	-
20020520 12:00/0521 00:00	-
20020522 00:00/0522 06:00	-
20020529 00:00/0529 12:00	-

*Continued on next page*

Table 7 – *Continued from previous page*

Start/End	GUMICS Magnetopause
20020530 06:00/0530 18:00	–
20020531 18:00/0601 00:00	–
20020602 18:00/0603 00:00	–
20020604 06:00/0604 12:00	–
20020605 06:00/0606 18:00	–
20020607 12:00/0608 06:00	+
20020609 00:00/0609 06:00	–
20020610 00:00/0610 06:00	–
20020611 00:00/0611 12:00	–
20020612 06:00/0614 00:00	–
20020614 18:00/0615 06:00	–
20020616 00:00/0616 12:00	+
20020620 00:00/0620 18:00	–
20020622 06:00/0622 18:00	–
20020704 12:00/0705 00:00	–
20020706 00:00/0706 12:00	+
20020709 00:00/0709 18:00	–
20020715 18:00/0716 12:00	–
20030105 06:00/0105 18:00	+
20030110 00:00/0110 12:00	+
20030112 12:00/0112 18:00	–
20030117 06:00/0117 12:00	+
20030121 06:00/0121 12:00	+
20030122 00:00/0122 06:00	–
20030126 18:00/0127 00:00	+
20030128 12:00/0128 18:00	+
20030129 00:00/0129 12:00	+
20030131 12:00/0201 00:00	+

Start/End	GUMICS Neutral Sheet
20020901 19:10/0901 23:54	–
20020906 14:07/0906 16:37	+
20020913 17:33/0913 20:06	+
20020918 12:47/0918 14:26	–
20020920 20:36/0921 02:13	+
20020928 02:58/0928 07:00	+
20021002 16:12/1002 23:52	–
20021014 12:34/1014 22:53	+
20021017 03:08/1017 04:11	–

<sup>1061</sup> **Table 8.** Intervals around the studied neutral sheet crossings in the tail. The Cluster SC3  
<sup>1062</sup> crossed the neutral sheet in all cases. The 2nd column shows whether the neutral sheet is visible  
<sup>1063</sup> in the GUMICS–4 simulations.